

Original Article

Cite this article: Clift PD, Kulhanek DK, Zhou P, Bowen MG, Vincent SM, Lyle M, and Hahn A (2020) Chemical weathering and erosion responses to changing monsoon climate in the Late Miocene of Southwest Asia. *Geological Magazine* 157: 939–955. <https://doi.org/10.1017/S0016756819000608>

Received: 31 May 2018

Revised: 15 April 2019

Accepted: 2 May 2019

First published online: 13 June 2019




Keywords:

weathering; erosion; monsoon; geochemistry; colour; IODP Site U1456

Author for correspondence:

Peter D Clift, Email: pclift@lsu.edu

Chemical weathering and erosion responses to changing monsoon climate in the Late Miocene of Southwest Asia

Peter D Clift^{1,2} , Denise K Kulhanek³ , Peng Zhou¹, Melanie G Bowen⁴, Sophie M Vincent¹, Mitchell Lyle⁵ and Annette Hahn⁶ 

¹Department of Geology and Geophysics, Louisiana State University, Baton Rouge, LA 70803, USA; ²Research Center for Earth System Science, Yunnan University, Kunming, Yunnan 650091, China; ³International Ocean Discovery Program, Texas A&M University, 1000 Discovery Drive, College Station, TX 77845, USA; ⁴Department of Geology and Geophysics, Texas A&M University, College Station, TX 77843-3115, USA; ⁵College of Earth, Ocean and Atmospheric Sciences, Oregon State University, Corvallis, OR 97331-5503, USA and ⁶MARUM, Centre for Marine Environmental Sciences, University of Bremen, Leobener Strasse, 28359 Bremen, Germany

Abstract

The late Miocene is a time of strong environmental change in SW Asia. Himalayan foreland stable isotope data show a shift in the dominant vegetation of the flood plains away from trees and shrubs towards more C4 grasslands at a time when oceanic upwelling increased along the Oman margin. We present integrated geochemical and colour spectral records from International Ocean Discovery Program Site U1456 in the eastern Arabian Sea to reconstruct changing chemical weathering and erosion, as well as relative humidity during this climatic transition. Increasing hematite/goethite ratios derived from spectral data are consistent with long-term drying after *c.* 7.7 Ma. Times of dry conditions are largely associated with weaker chemical alteration measured by K/Rb and reduced coarse clastic flux, constrained by Si/Al and Zr/Al. A temporary phase of increased humidity from 6.3 to 5.95 Ma shows a reversal to stronger weathering and erosion. Wetter conditions can result in both more and less alteration due to the nonlinear relationship between weathering rates, precipitation and sediment transport times. Trends in relative aridity do not follow existing palaeoceanographic records and are not apparently linked to changes in Tibetan or Himalayan elevation, but more closely correlate with global cooling. An apparent opposing trend in the humidity evolution in the Indus compared to southern China, as tracked by spectrally estimated hematite/goethite, likely reflects differences in the topography in the Indus compared to the Pearl River drainage basins, as well as the generally wetter climate in southern China.

1. Introduction

The response of landscape to climate forcing remains a controversial topic but one that is critical for deconvolving the competing effects of surface processes compared to tectonic forces in controlling continental erosion and chemical weathering fluxes (Burbank *et al.* 2003; Reiners *et al.* 2003; Riebe *et al.* 2004). This issue is of wide significance because of the proposed links between intensified chemical weathering and global climate, largely modulated through the drawdown of atmospheric CO₂ (a noted greenhouse gas) that can drive global cooling (Raymo & Ruddiman, 1992; Berner & Berner, 1997). In this study we examine the response of the Indus drainage basin to a well-documented climatic transition in SW Asia at *c.* 8 Ma in the late Miocene (Kroon *et al.* 1991; Prell *et al.* 1992). Current models predict that higher humidity and warmer conditions should be associated with higher degrees of chemical weathering because such conditions speed up the rate of chemical breakdown of pristine mineral species into weathering products such as clays (Kump *et al.* 2000; West *et al.* 2005). More intense weathering also increases the relative loss of water-mobile elements (e.g. Na, K, Sr) from bulk sediment, causing net change in composition (Nesbitt *et al.* 1980).

We conducted this study on sediments from the Arabian Sea because this deep sea basin is supplied with a strong flux of siliciclastic sediment, largely derived from the western Himalaya, Karakoram and associated ranges (Fig. 1) (Clift *et al.* 2001), which in turn are heavily influenced by monsoon rains, that are especially focused on the southern flank of the orogen (Bookhagen & Burbank, 2006). Erosion of the western Himalaya has been linked to monsoon intensity over a variety of timescales (Clift *et al.* 2008*a, b*), although the region also receives moisture from the west in the winter season via the Westerly Jet (Karim & Veizer, 2002). The Indus drainage basin is noted for being particularly seasonal, especially compared to the wetter eastern Ganges – Brahmaputra basin, a contrast that dates back into the Miocene (Vögeli *et al.* 2017).

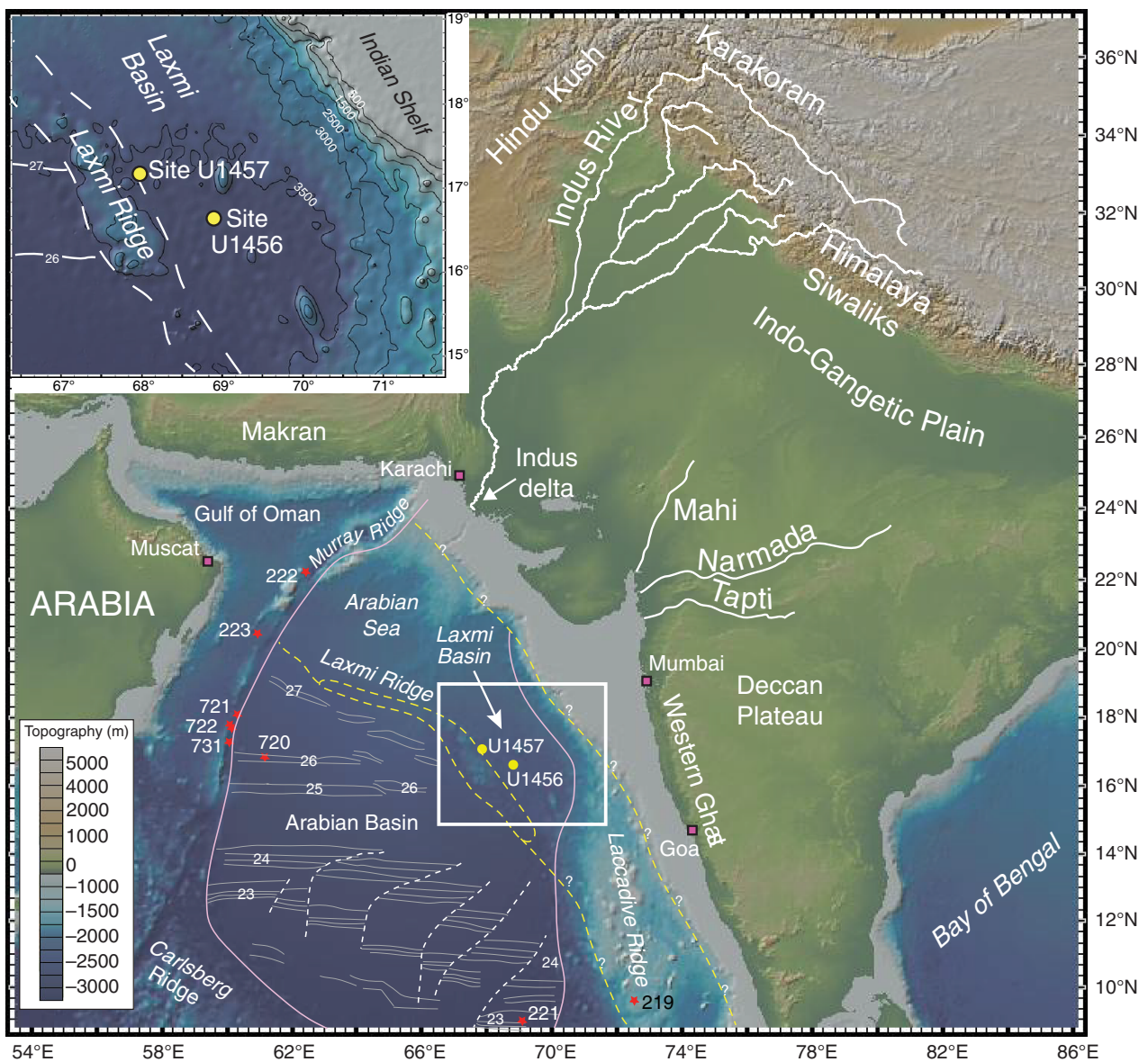


Fig. 1. Shaded bathymetric map showing the location of the boreholes (yellow dots) considered in this study as well as the major geographic features discussed in the text. Red stars show the locations of existing scientific boreholes. Pink squares show locations of major cities in the area. Magnetic anomalies shown as thin white lines are from Miles and Roest (1993). Dashed yellow lines show the continent–ocean transition. Dashed white lines show oceanic fractures zones. Base map is from GeoMapApp. Modified from Pandey *et al.* (2016b).

The Indus Basin has been the subject of several earlier regional palaeoclimatic studies that allow us to readily compare erosion and weathering proxies with independently derived climatic data.

Earlier scientific drilling in the western Arabian Sea has established that the late Miocene was a time of significant climate change. A marked increase in the relative abundance of *Globigerina bulloides*, a planktonic foraminifer today associated with coastal upwelling on the Arabian Oman margin at times of strong summer monsoon winds (Curry *et al.* 1992), indicated initiation of the modern wind system at *c.* 8 Ma (Kroon *et al.* 1991; Prell *et al.* 1992). More recent work now highlights initial changes after 13 Ma (Gupta *et al.* 2015; Betzler *et al.* 2016); however, this does not diminish the potential importance of the 8 Ma transition. Results from terrestrial studies also emphasize the importance of this period as a time of environmental transition. Stable carbon isotope data from soil carbonates in the Pakistani parts of the

Himalayan foreland also show a trend to more positive $\delta^{13}\text{C}$ values at a similar time (Quade *et al.* 1989). This isotopic shift was interpreted to indicate a change from a tree- and shrub-dominated C3 vegetation assemblage to a grass-dominated C4 one. This floral change was also recorded, albeit occurring slightly later, in the NW Indian parts of the Indus Basin (Singh *et al.* 2011). Although initially interpreted to reflect a strengthening of summer rains linked to monsoon initiation, this change in vegetation is now generally considered to indicate a drier climate, or at least an increase in seasonality, which is also a feature of the monsoon (Tada *et al.* 2016). It is clear that those proxies that are linked to terrestrial weathering and erosion and thus partly influenced by continental rainfall and those proxies linked to oceanographic biogenic productivity are not necessarily in sync or agreement with one another, making a simple testing of environmental change harder to achieve (Clift, 2017).

Erosion records based on seismic data from the Arabian Sea show a decrease in erosion from the middle to the late Miocene and into the Pliocene at a time when sparse geochemical data from drilled sections on the Indus Shelf point to reduced chemical alteration (Clift *et al.* 2008b). This trend was interpreted to reflect a progressive drying of the climate in the Indus Basin after *c.* 14 Ma until *c.* 3 Ma, but this reconstruction and its interpretation remains controversial. Although heavier summer rains can favour faster erosion (Clift *et al.* 2008b), the relationship is not linear because heavy but infrequent rain in arid regions can drive faster erosion during flash floods, especially when there is little vegetation to hold soil in place (Burbank *et al.* 1993; Molnar, 2001; Giosan *et al.* 2017). Likewise, heavier rain need not cause chemical alteration to increase because strong rains can increase river discharge and reduce transport times between source and sink. Thus, even if rates of weathering increased, the total degree of alteration of the sediment deposited at a given time could decrease if transport time reduced sufficiently.

Here we examine the history of chemical weathering and environmental aridity in the Indus Basin from 8.5 Ma to 5.5 Ma using cores collected from International Ocean Discovery Program (IODP) Site U1456 in order to assess the response to and nature of the climatic transition during the late Miocene. Although records spanning this time period are known onshore within the Siwalik Group sedimentary rocks of the Himalayan foreland basin (Fig. 1) (Tauxe & Opdyke, 1982; Burbank *et al.* 1996; Najman, 2006), each of the existing sections in that area essentially preserves the output of the local major tributary as it leaves the mountain front. While that is useful, these rocks do not provide a terrestrial basin-wide record. Moreover, the Siwalik Group sections represent a proximal record deposited upstream of the flood plains where much of the weathering may occur (Lupker *et al.* 2012) and where most of the vegetation is assumed to grow. IODP Site U1456 thus provides a unique, newly available opportunity to examine erosion and weathering in the type area for which the SW monsoon is known (Pandey *et al.* 2016a).

In this study we combine two scanning methods to derive high-resolution weathering, erosion and environmental records. X-ray fluorescence (XRF) core scanning was used on split core sections to collect a suite of major and select trace elements that were used to calculate weathering and erosion proxies. We supplement these data with diffuse reflectance spectroscopy (DRS) measurements used to define the relative abundance of the environmentally sensitive minerals hematite and goethite (Schwertmann, 1971), which have been used to constrain regional aridity in marine cores (Balsam *et al.* 1997; Giosan *et al.* 2002), including previous monsoon studies (Clift *et al.* 2008b). Our study is unique in comparing these two datasets at high resolution over a critical climatic transition.

2. Geologic setting

IODP Expedition 355 sampled sediments from the Indus Fan deposited within the eastern Arabian Sea (Pandey *et al.* 2016b). IODP Site U1456 is located in the Laxmi Basin, which is separated from the main Arabian Basin by the Laxmi Ridge (Fig. 1). The Laxmi Basin first formed during the latest Cretaceous when India began to separate from the Seychelles as seafloor spreading between these continental blocks initiated (Bhattacharya *et al.* 1994; Pandey *et al.* 1995). Following the onset of India–Asia collision, likely *c.* 50–60 Ma (Najman *et al.* 2010; DeCelles *et al.* 2014), the uplift and erosion of the Himalaya has resulted in the delivery

of large sediment volumes to the Indus Submarine Fan. The Indus Fan is the second largest sediment body on Earth, estimated to comprise $4\text{--}5 \times 10^6 \text{ km}^3$, with a maximum thickness exceeding 11 km under the Indus Shelf, but much less in the Laxmi Basin (Kolla & Coumes, 1987; Clift *et al.* 2001).

Site U1456 lies in the central part of the Laxmi Basin above the carbonate compensation depth (CCD) so that it was possible to date the age of sedimentation using a combination of nannofossil and foraminiferal biostratigraphy, coupled with magnetostratigraphy that provides a relatively robust age model (Routledge *et al.* 2019).

The primary source of sediment to the core site is believed to be the Indus River, with lesser inputs from peninsular rivers such as the Tapti and Narmada. Initial shipboard petrographic-based interpretations of the sediments suggested that there were limited amounts of sediment delivery from Western India, mostly in the youngest parts of the section (Pandey *et al.* 2016a). Bulk sediment Nd isotope measurements from muddy sediments can be compared with more proximal deposits to determine if a sediment is probably Indus-derived or not (Clift *et al.* 2018). Figure 2 shows Nd isotope values from the three samples that fall within the analysed section. The lower two are within the ‘probable Indus-derived’ field, with one at 540 m below seafloor (mbsf) (~6.8 Ma) that could be influenced by run-off from the Indian peninsula margin. The same study also dated zircon grains from sands at Site U1456 which were revealed to be all Indus-derived, including one from the section studied here (U1456D-13R-1). Nd was analysed at higher resolution at nearby Site U1457 and was shown to be dominantly Indus-derived over the time interval considered here, and that provenance within the basin was also mostly stable. Although we cannot exclude influence from the Indian peninsula, the evidence suggests that the bulk of the siliciclastic sediment considered here is from the Indus River catchment.

Regional wind patterns do not now favour aeolian transport from Arabia, but possibly from modern Somalia. Sediment trap data in the modern basin show aeolian sedimentation reducing to the east away from Arabia (Pease *et al.* 1998). The highest sedimentation rates occur during the winter and spring, under the influence of the South Asian winter monsoon bringing material from the Thar Desert. However, the Thar Desert is itself derived from the Indus delta (East *et al.* 2015), which makes resolving aeolian vs water-borne sediment difficult. The age of the Thar Desert is not well known, but it is at least 200 ka old (Singhvi *et al.* 2010). It is unknown if it existed in the generally warmer, wetter conditions of the Miocene. Sedimentation rates over the studied interval are *c.* 10 cm ka^{-1} . With an average dry density of *c.* 1.6 gm cm^{-3} this is equivalent to *c.* $160 \text{ g cm}^{-2} \text{ ka}^{-1}$ of total siliciclastic sedimentation, mostly in the form of clay. In contrast, modern sediment traps offshore western India indicate average aeolian sedimentation of $0.29\text{--}1.05 \text{ g cm}^{-2} \text{ ka}^{-1}$ (Honjo *et al.* 1999), meaning that the aeolian contribution is a very small fraction of the total deposit.

The sedimentary facies of the studied material are dominantly hemipelagic shales and calcareous mudstones, with only minor amounts of fine sand or silty graded interbeds interpreted as turbidite deposits. Nonetheless, the studied materials are interpreted to be either the product of hemipelagic hypopycnal plumes derived from the Indus River mouth, or more likely distal turbidites with carbonate biogenic background sedimentation that occasionally dominates deposition at the site (Pandey *et al.* 2016a). Relative reduction in siliciclastic sediment flux might represent times of reduced Indus discharge, but could equally reflect avulsion of the major fan depositional lobes from the Laxmi Basin into the

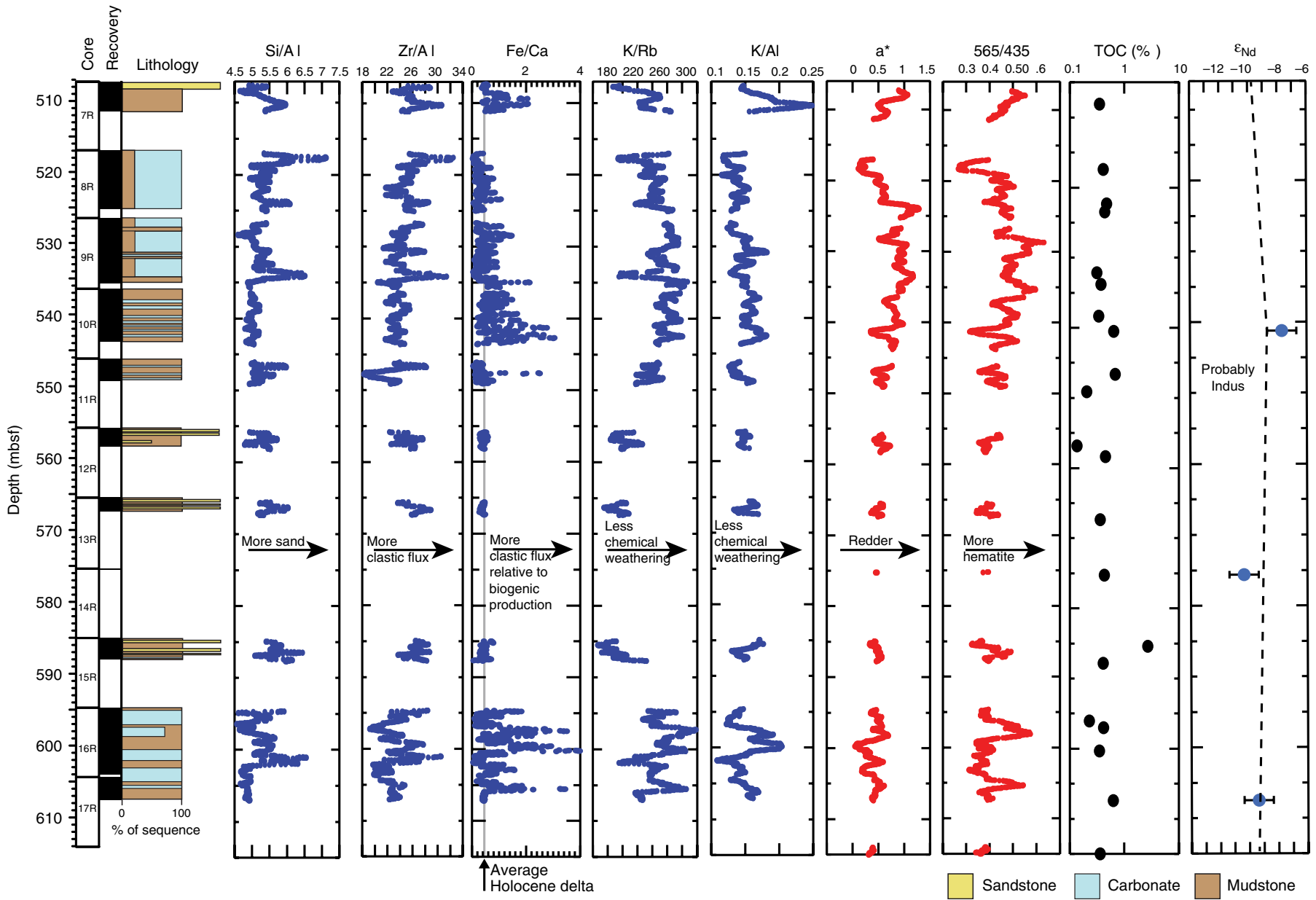


Fig. 2. Downhole variations in key geochemical proxies used in this study showing their relationship to the recovered lithologies. Total organic carbon values are from Pandey *et al.* (2016a). ϵ_{Nd} values are from Clift *et al.* (2018). Ratios are calculated from wt % of oxides.

Arabian Basin, or a bloom in biogenic productivity offshore western India diluting the clastic flux.

3. Analytical methods

3.a. Spectral reflectance

DRS data from Site U1456 sediment were collected at the IODP Gulf Coast Repository (GCR) in College Station, Texas (USA), using a handheld Minolta CM-2002 Spectrophotometer between depths of 507.32 and 726.54 mbsf. Data collected with the Ocean Optics USB4000 spectrophotometer on the Section Half Multisensor Logger (SHMSL) during Expedition 355 are considered to be unreliable at short wavelengths (<500 nm) due to use of a light source with little power at those values. This resulted in a failure to capture the first-derivative peak at 435 nm, although longer wavelengths and proxies such as a^* (redness) are considered reliable. The first-order derivatives at 565 nm and 435 nm were calculated from the data collected with the Minolta CM-2002 and their ratio was used to represent the relative contents of hematite and goethite. This ratio has previously been used as a proxy of relative humidity (Balsam *et al.* 1997; Giosan *et al.* 2002; Ji *et al.* 2002). Hematite formation is favoured in dry, warmer environments (Schwertmann, 1971), whereas goethite is generally associated with cooler, wetter environments and is often favoured by the presence of minor organic matter (Schwertmann, 1971; Sangode & Bloemendal, 2004).

The principle of DRS measurement involves illuminating a sediment surface with a known source and collecting the reflected light in an integration sphere. The normalized reflected signal must be calibrated over the measured wavelength range according to the spectra of pure white and black standards, representing 100 % and zero reflectance, respectively. DRS measurements across the entire wavelength spectrum of visible light (400–700 nm) are a standard physical properties measurement performed by Ocean Drilling Program (ODP) and IODP since the late 1990s, and the Minolta CM-2002 instrument employed in the measurement of material from IODP Site U1456 provides a percentage reflectance spectrum with a wavelength resolution of 10 nm. DRS scanning was performed at 2 cm intervals throughout the cores where material was available and where a flat area of core could be found so that the sensor of the Minolta Spectrophotometer was fully in contact with the core surface at the time of measurement. Interference from outside light was avoided in order to increase the accuracy of the reflectance data. The archive half was carefully scraped and rewrapped with polyethylene prior to scanning. Data from the scanning are available online as Supplementary Table 1 (<https://doi.org/10.1017/S0016756819000608>).

3.b. XRF core scanning

XRF geochemical core scanning was conducted at the IODP GCR using a third-generation Avaatech XRF scanner with a Canberra X-PIPS (passivated implanted planar silicon) silicon drift detector (SDD), Model SXD 15C-150-500 150 eV resolution X-ray detector. Data considered in this study were collected between depths of 507.40 and 607.28 mbsf. The XRF scanner is configured to analyse the split surface of core section halves for elements between aluminium (Al) and uranium (U) in the periodic table. The X-ray tube and detector apparatus are mounted on a moving track so that multiple points along the length of a core section can be analysed in a single scanning run and multiple scans at different energies can be automatically programmed. A basic description of first- and

second-generation Avaatech scanners is given in Richter *et al.* (2006).

For the Site U1456 XRF scans, each core section was removed from refrigeration at least 2 hours before scanning and scraped to clean and level the split core surface. The surface was covered with 4 μm thick Ultralene plastic film (SPEX Centriprep, Inc.) to prevent contamination of the X-ray detector. The Ultralene film was rolled onto the dry surface of the core section and taped to the plastic core liner to ensure that it remained in place. After the core section was placed in the Avaatech core scanner, the film was examined for ridges/undulations and smoothed using a Kimwipe or additional tape. No water was added to the core surface, and because the work was undertaken several months after core recovery there was no free water remaining on the cut surface. Measurements were taken at 2 cm intervals during two separate scans at different voltages (10 kV and 30 kV). The 10 kV scan (with X-ray tube current of 800 μA , no filter, and 15 s detector live time) collected data for elements Al, Si, S, Cl, K, Ca, Ti, Mn and Fe. The 30 kV scan (with X-ray tube current of 1000 μA , Pd-thick filter and 20 s detector live time) collected data for elements Ni, Cu, Zn, Br, Rb, Sr, Y, Zr, Nb, Mo, Pb and Bi. For both scans, the X-ray illumination area was set at 1.0 cm in the downcore direction and 1.2 cm in the cross-core direction, and the scan was run down the centre of the split core section.

XRF data presented here were reduced using the Normalized Median-Scaled (NMS) method presented in Lyle *et al.* (2012). For this study, the XRF data were scaled to a sediment composition model derived from average greywacke, modified to account for calcium carbonate measured on discrete samples taken during the expedition. To do this, the median of the raw counts value for each element was set to the sediment model per cent. The raw count value for each element was converted to a percentage by dividing it by the median raw count value and then multiplying by the median model elemental abundance. These data were then normalized such that the major rock-forming oxides summed to 100 %, which eliminates variability caused by uneven surfaces, variations in porosity and variations in XRF source intensity (Lyle *et al.* 2012). Minor and trace elements were multiplied by the same factor. A more detailed account of data reduction for the Expedition 355 XRF data is given in Lyle *et al.* (2018).

Discrete samples from these cores were also analysed by conventional (benchtop) XRF as part of a study to determine if handheld XRF measurements yielded robust results that can be used for calibration of core scanning data (Hahn *et al.* 2019). It is important to note that the core scanning measurements were made along the middle of the archive half-core sections, with the sampling window set to 10 mm in the downcore direction and 12 mm across core. This measurement samples only the uppermost few millimetres of the sediment. Samples for conventional XRF measurements were taken from the working half-core sections over a 1 cm interval spanning from the outer edge of the core to just short of the middle of the core (Fig. 3b), and then freeze-dried and homogenized using a mortar and pestle. Replicate measurements on the same samples yielded an accuracy within 1 % and standard deviation of 2 % for the conventional XRF measurements (Hahn *et al.* 2019). Therefore, the conventional and core scanning XRF measurements are not done on the same piece of sediment and while they should generally correlate, outliers are likely, especially when thin or discontinuous beds are present. Figure 3a compares our NMS XRF data to the conventional XRF discrete sample measurements for Al, K, Si and Rb to demonstrate that there is generally good correlation between these methods and that we can use the

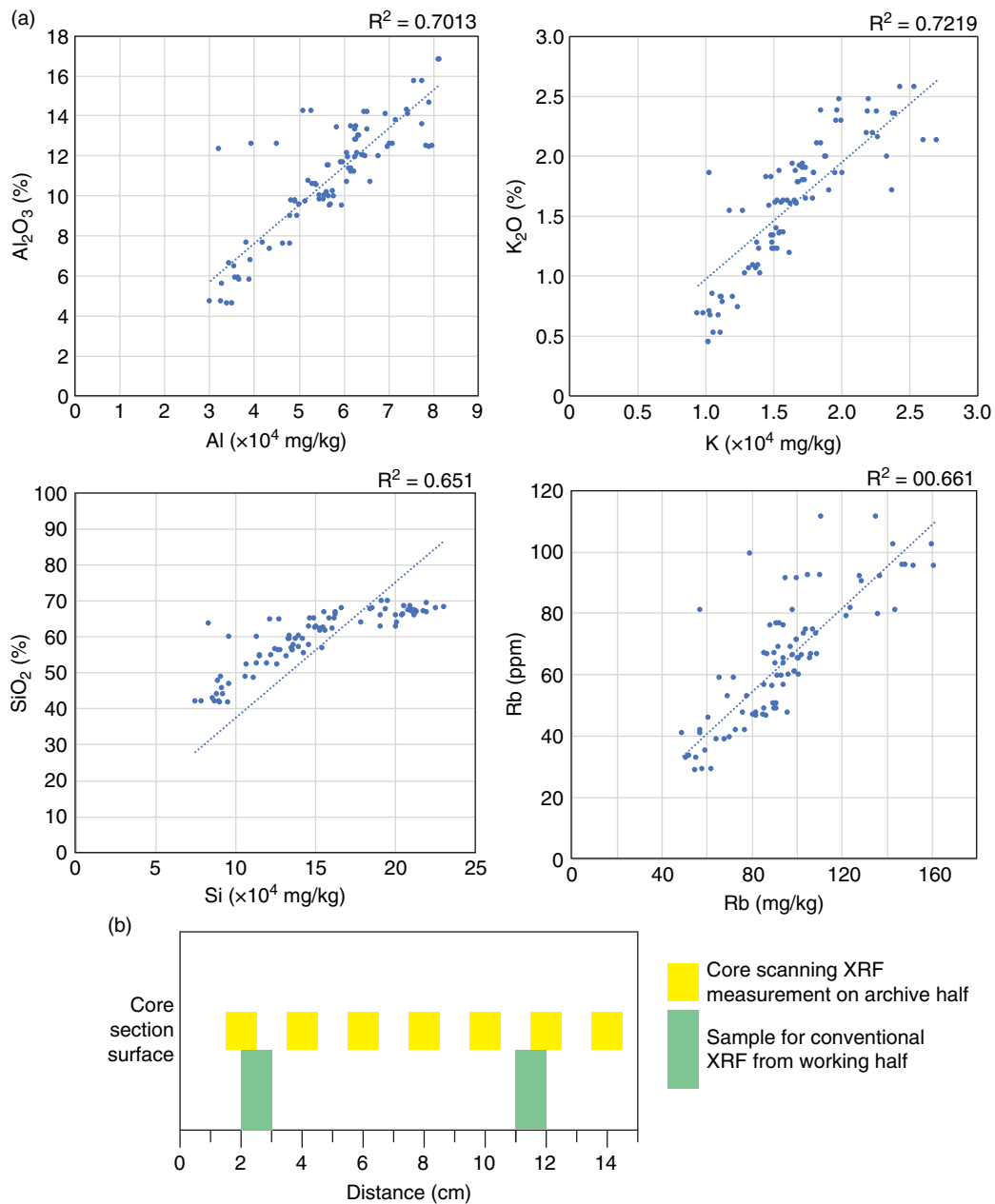


Fig. 3. (a) Cross-plots comparing the NMS XRF data (y-axes) to conventional XRF measurements on discrete samples (x-axes; data from Hahn *et al.* 2019) for Al, K, Si and Rb. A trendline through the origin is shown for each plot, with the correlation coefficient shown above each graph. (b) Schematic diagram showing core section surface and position of core scanning XRF measurements (yellow rectangles) done on archive half-cores relative to discrete samples for conventional XRF measurements (green rectangles) taken from working half-cores. The measurements are done on the same general interval of the core but not on the same sediment, which results in some scatter between datasets.

significantly higher-resolution core scanning data to examine downhole trends. This comparison shows that the correlations are quite good, with $R = 0.70$ for Al, 0.72 for K, 0.65 for Si and 0.66 for Rb. The Si data show an interesting distribution where the NMS method overestimates SiO_2 per cent for lower concentrations and underestimates it for higher concentrations. We suspect that this is in part related to grain-size variations, as samples with higher SiO_2 content are generally sandier (Fig. 4). Although the presence of water on the core surface degrades the quality of analysis of light elements such as Al, Si and K by core scanning (Kido *et al.* 2006), this is not a critical issue in this study as demonstrated

by the relatively good fit between the core scanning and conventional XRF measurements, which argues against major systematic error (Hahn *et al.* 2019) (Fig. 3b). These plots also allow average uncertainties to be assessed based on the degree of scatter away from the line of best fit between the two datasets. Here we employ elemental ratios as proxies to observe qualitative changes downhole. Other studies have demonstrated that even though different calibration methods yield variations in overall quality of the calibrated dataset, downhole trends do not change and therefore these data can be used to make qualitative inferences, regardless of calibration method (e.g. Weltje *et al.* 2015).

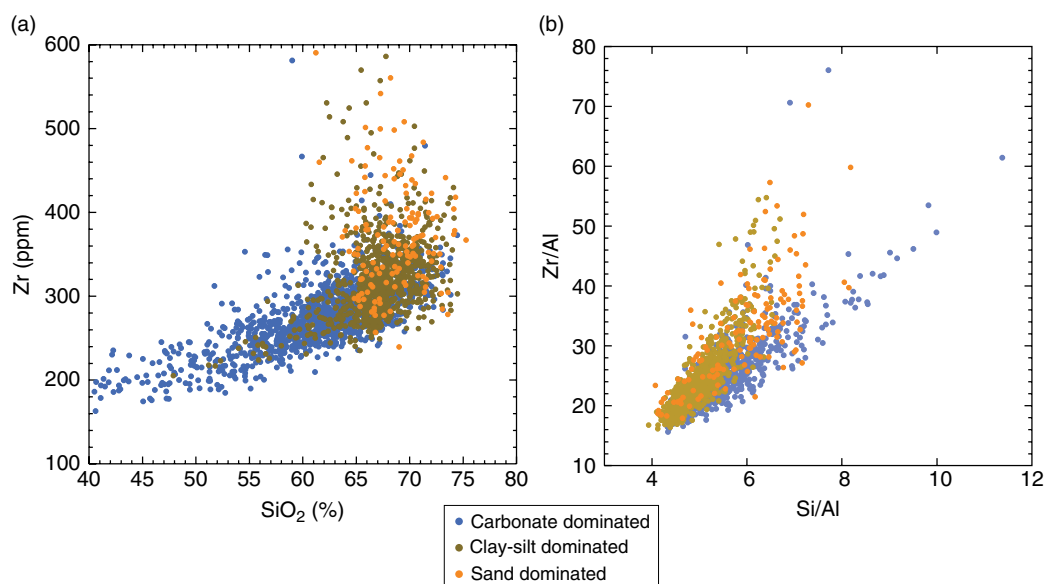


Fig. 4. Cross-plot of (a) Zr against SiO_2 concentrations and (b) Zr/Al vs Si/Al, showing correlation indicative of most zircon being held in the sandier quartz-rich layers.

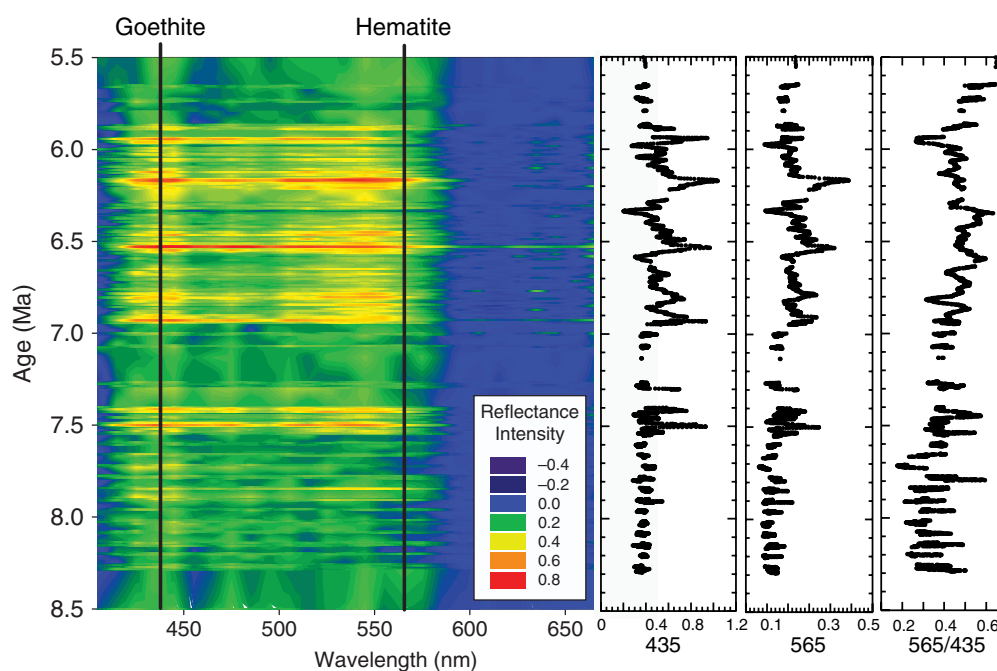


Fig. 5. Plot showing the strength of the spectral first derivative for all measured wavelengths at Site U1456 for the age range addressed in this study. Note the generally strong hematite and goethite peaks.

4. Spectral reflectance data and proxy interpretation

Before plotting and utilizing the 565/435 (hematite/goethite) environmental proxy, it is critical to confirm the existence of these first derivative values, i.e. that there are well defined hematite and goethite peaks in the spectral data. If either of these minerals is absent then the value of the proxy is itself questionable. A relatively strong first-derivative value at these particular wavelengths serves as evidence for a detectable amount of these minerals. We calculated the 565/435 value by determining the first-order derivative every 5 nm from the 400 nm wavelength to 700 nm. A three-dimensional plot, containing depositional age, wavelength, as well as the first-derivative values, was created by using the software SigmaPlot in

order to assess the strength of the signal (Fig. 5). This approach demonstrates that the first derivative at both 435 nm and 565 nm is quite strong over most of the interval dated between 5.5 and 8.5 Ma, although there is little hematite in sediments dated from 8.3 to 7.7 Ma. Simple two-dimensional plots of the strength of the 435 and 565 nm first derivatives show variable but positive values through the entire studied section, implying that there is signal for both minerals that allow effective use of this proxy (Fig. 5).

To confirm that the 565/435 proxy is a robust tool, we further compared this with the a^* (redness vs greenness) value from the same analyses because this particular measurement is relatively easily collected and considered generally reliable. Redness should

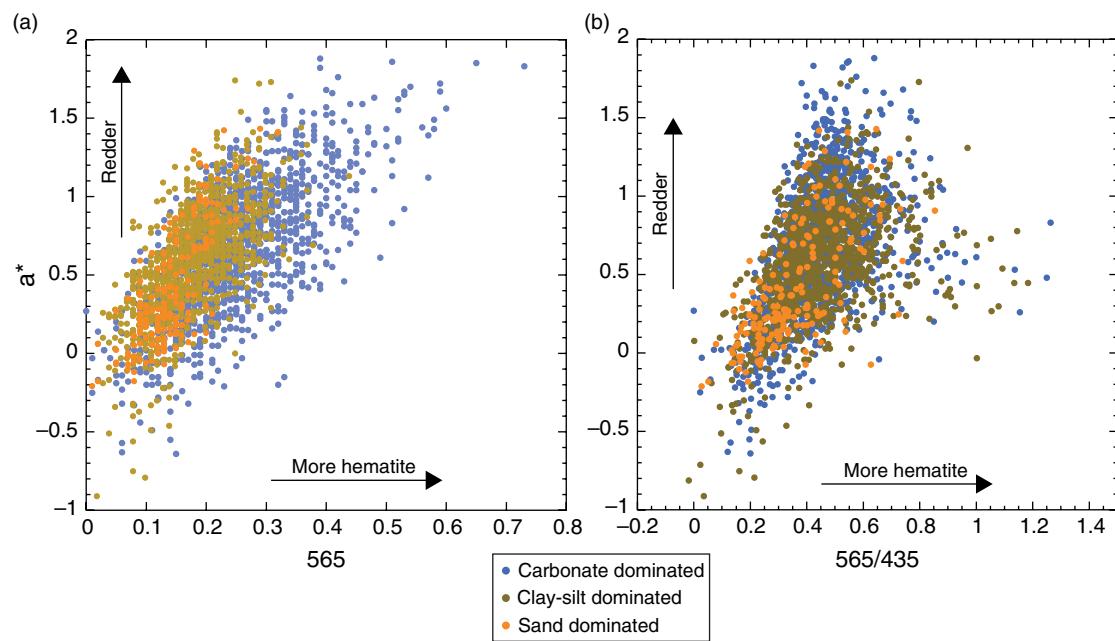


Fig. 6. Cross-plot of (a) a^* vs 565, and (b) a^* vs 565/435 for all data from 5.5 to 8.5 Ma from Site U1456.

at least partially reflect hematite content and thus co-vary with both 565 and the 565/435 proxy provided that other mineral phases do not dominate in controlling redness. Figure 6a shows that there is a generally positive correlation indicating that redder sediments tend to have higher 565 ($R = 0.6700$), especially for sand-rich sediment ($R = 0.7819$). Higher a^* values also correlate with higher 565/435 values and thus relatively more hematite (Fig. 6b). The correlation coefficient in the latter case is not as high ($R = 0.4549$) but is best in sandy sediment ($R = 0.6672$). This suggests that 565/435 is partly controlled by relative hematite content and that there are measurable amounts of hematite throughout the section.

Care also needs to be taken in using hematite/goethite as an environmental proxy because the preserved hematite and goethite contents of the sediments can be influenced by diagenesis as well as original mineralogy during deposition. Although iron oxide reduction is typically limited to the upper metre of the sediment column, rock magnetic studies of sediments from the Bengal Fan highlighted the possible role of organic carbon in controlling pyrite formation and the degree of deeper diagenesis, which in turn influences the hematite and goethite abundance. However, the Bengal Fan is systematically more efficient in carbon burial compared to the Indus (Galy *et al.* 2007). To check that organic carbon is not driving significant reduction and affecting the measured hematite/goethite, we plot total organic carbon against the 565/435 values and note the lack of any coherent variation (Fig. 2). Organic matter was interpreted to be of mixed marine and terrestrial sources, but with a modest bias towards terrestrial sources, based on the total organic carbon and total nitrogen contents (Pandey *et al.* 2016a).

5. Major element data and proxy interpretation

Si/Al is considered to be a proxy for the sandiness of the sediment because quartz is rich in silica, whilst clay is rich in aluminium (Hu *et al.* 2016). These cores are drilled in a turbidite-rich submarine fan dominated by siliciclastic sediment and biogenic carbonate,

as revealed by core descriptions and microscopic analysis (Pandey *et al.* 2016a). There is negligible biogenic silica, mostly in the form of diatoms, radiolarians and minor sponge spicules, with the former limited to the top few metres of the stratigraphy in much younger sediments than considered in this study. Microscopic inspection of sediments in the studied interval shows either no siliceous biogenic material or trace numbers of sponge spicules. Because Si/Al is a proxy for quartz sandiness and greater current power is required to transport coarser-grained sand compared to fine clay-rich sediment, this proxy can be used as an indicator of discharge power linked to run-off and the erosion of coarse material in the source regions. However, we recognize that hydrodynamic sorting occurs every time the sediment is reworked and redeposited, including in any turbidite deposit, so that its reliability as a proxy for terrestrial processes must be considered suspect, despite the fact that most of the stratigraphy comprises hemipelagic muds and carbonates. For those sparse sandy units that were deposited as turbidites, the grain-size characteristics are more controlled by the location of the drill site relative to the main depocentre.

Zr/Al is another proxy for siliciclastic flux because Zr is largely present in zircon grains. Geochemical analysis of Indus delta sediments indicates that sediment $<63 \mu\text{m}$ is more Zr-rich than the coarser grain-size fraction, with average contents of 310 ppm for $<63 \mu\text{m}$ compared with 149 ppm for 63–125 μm and 261 ppm average of 125–250 μm (Jonell *et al.* 2018). However, this study did not distinguish between clay- and silt-sized material, and zircon grains are typically part of the coarser silty sediment because of their high density, rather than of clay-rich sediment (Olde *et al.* 2015). Zr does not reflect dispersed volcanic glass shards or the presence of visible volcanic ash layers but must be siliciclastic and continental in origin as volcanic glass shards were not seen in the studied interval. Zircon is present in most continental igneous and sedimentary rock units and might be expected to increase in concentration when erosion from these sources increased and the eroded material became more silty and less clay-rich. The proxy assumes that the sources do not change their relative yield of silt, sand and clay through time. Nd isotope data suggest that

provenance does not change much over the time span of this study (Clift *et al.* 2018), so this potential influence can be discounted. Zr/Al has been also been used as a silt grain-size proxy, and as a proxy for current strength during transport and sedimentation (Bahr *et al.* 2014). This in turn is linked to discharge and stream power that control rates of erosion in river valleys (Whipple & Tucker, 1999). Earlier studies from Quaternary sediments in the Arabian Sea show that coarser-grained turbidite silts and sands have higher Zr/Al and Si/Al values than interbedded mudstones (Schnetger *et al.* 2000). When continental erosion is strong and discharge from the river mouth is high, then the proportion of such siliciclastic sediments in the submarine fan is higher than when erosion is slow and the deep-sea sediment is dominated by clay. In this study, Zr/Al is used as a proxy for relative silt content, usually associated with higher fluvial discharge.

Fe/Ca was used as a proxy for siliciclastic flux relative to biogenic carbonate productivity because in many marine cores the amount of siliciclastic Ca is relatively low and the CaO content is mostly a function of biogenic carbonate (Govin *et al.* 2012). Carbonate is present throughout the section studied, at levels as low as 5.4 % to as high as 47.8 % (Pandey *et al.* 2016a) so that CaO concentrations are almost always greatly in excess of the average upper continental crust concentration of 3 % (Taylor & McLennan, 1995). Diagenesis can affect the Fe contents of sediment through reduction, but this process occurs in the top tens of cm of the sediment column (Burdige, 1993) and is not relevant on the depth range and scale considered here. Robinson *et al.* (2000) indicated that sedimentation rate and organic material content can be important in controlling the rate of Fe diagenesis. A stronger diagenetic process is associated with a faster sediment flux and a high (>0.5 %) organic content, both of which are low in the studied section, averaging 3.7 cm ka⁻¹ and mostly <0.5 %. Although more advanced remobilization is possible at greater depths, this is considered unlikely here in view of the shallow depths of burial and the lack of evidence for Fe mobilization and redistribution. We compare our data with the average of CaO = 7.9 % and Fe/Ca = 0.75 measured by conventional means in the Holocene delta (Clift *et al.* 2010). Fe/Ca values lower than this reflect biogenic production, whereas higher values may point to times of greater erosional flux. This comparison implies that this Fe/Ca proxy is not driven by compositional variations within the siliciclastic fraction. K/Rb and K/Al plot relatively water-mobile potassium against less water-mobile elements in order to quantify the degree of leaching of water-mobile potassium from the sediment prior to deposition (Nesbitt *et al.* 1980; Lupker *et al.* 2013). Both are proxies for the degree of chemical alteration. We assume that most of the alteration occurs prior to sedimentation, probably onshore in continental flood plains, rather than during diagenesis. Rb is mostly left in weathering profiles after leaching and is only transported to the ocean if the soils are then mass-wasted. Rb is rich in biotite but is also preferentially retained on clay minerals during chemical breakdown compared to K. However, Rb in K-feldspar and biotite is known to be more readily mobilized than K during weathering (Nesbitt *et al.* 1980; Blum & Erel, 1997), which can result in a complex weathering response, depending on the source rock lithologies and the time-scales of weathering and transport. Hu *et al.* (2016) showed that on millennial timescales K/Rb was a better tracer of weathering intensity in the northern South China Sea but that on longer scales K/Al provided a more coherent signal in that area. We plot both of these proxies because of their different sensitivities under the stress of chemical weathering. Although many studies prefer K/Al

(Clift *et al.* 2008b; Lupker *et al.* 2013; Clift *et al.* 2014; Wan *et al.* 2017), there are examples where this is relatively invariable, whereas K/Rb can highlight weaker degrees of chemical weathering (Hu *et al.* 2016).

6. Results

We plot a series of geochemical and spectral proxies against depth in mbsf in order to assess how they relate to lithology. There is greater variation with depth in K/Rb compared to K/Al (Fig. 2). In particular, K/Rb is relatively high below 595 mbsf, as well as between 515 and 545 mbsf. These are sections of the core with significant amounts of carbonate, as well as clay-rich mudstone. K/Al shows a very high value at c. 510 mbsf, but is otherwise somewhat variable, although there is a subtle long-term decrease in values between 545 and 517 mbsf spanning a carbonate-rich interval.

Si/Al and Zr/Al show similar trends with depth, which are quite different from those shown by Fe/Ca (Fig. 2). Not surprisingly Fe/Ca is highest in carbonate-poor parts of the section, although it is not clear if this reflects high clastic sediment delivery or low biogenic carbonate productivity. This ambiguity is not applicable to Si/Al and Zr/Al, because these only reflect the composition of the siliciclastic fraction. Both proxies have relatively high values that peak at c. 602 mbsf, with another sharp increase above 535 mbsf, remaining variable but generally high as shallow as 517 mbsf. Both proxies show short-lived peaks over that interval that suggest strong influxes of siliciclastic material from the continent, despite the fact that much of this part of the section is relatively carbonate-rich. This merely indicates that the siliciclastic fraction of the carbonate-dominated sediments is quite sandy and not muddy. Other maxima correlate with thin-bedded sand units between 585 and 588 mbsf. In contrast, variation in a* shows a relatively straightforward increase up-section from 607 to 524 mbsf, above which it decreases to a minimum at c. 518 mbsf, before increasing again towards the top of the studied section. The 565/435 values show similarities with the a* record, as might be expected from their overall general correlation (Fig. 2), although some of the maxima and minima are more extreme in this proxy. In general the record appears to show increasing amounts of hematite relative to goethite, with a maximum value reached at ~530 mbsf where the sediment is relatively carbonate-rich.

7. Discussion

We assigned samples to one of three major sediment types using the shipboard visual core description logs: clay- and silt-dominated (<63 µm), sand-dominated (>63 µm) and carbonate-dominated (Pandey *et al.* 2016a), where 'dominate' indicates sediment comprising more than 50 % of the total described interval. Because the descriptions did not consider variations of <10 cm thickness it is possible to have thin beds of other lithologies interbedded within a dominant sediment type, although this was not common here. The plot of a* against 565/435 shows that the silt/clay and carbonate-rich sediments span a similar range of redness and hematite contents, but that sandy sediment is preferentially associated with low hematite/goethite values (Fig. 2). This could mean that sandy sedimentation is associated with more humid environmental conditions, or that sand is associated with low concentration of iron oxides. Nonetheless, the general covariation between redness (a*) and hematite/goethite suggests that both parameters are controlled by the same process.

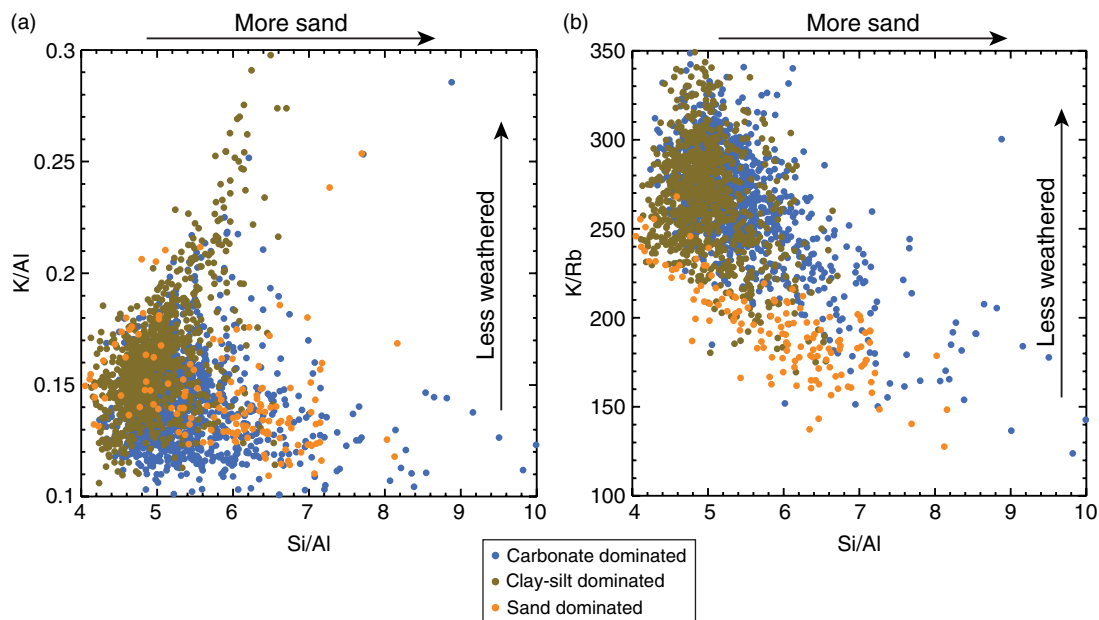


Fig. 7. Cross-plots of (a) K/Al and (b) K/Rb vs Si/Al, which we use as a grain-size proxy. K/Al shows no clear trend while K/Rb shows a weak negative correlation. Ratios are calculated from wt % of oxides.

Links between lithology and chemistry are explored further by plotting Zr against SiO₂, which demonstrates a rough positive correlation (Fig. 4a; $R = 0.5951$), as might be expected given that Zr/Al is designated as a silt proxy and Si/Al as a proxy for coarser quartz-bearing sediment relative to clay. This is especially clear for the carbonate-dominated sediment ($R = 0.6717$). The linear correlation is most robust for SiO₂ concentration <65 %, above which some values of Zr increase very sharply in a nonlinear fashion, especially for both sand and silt/clay-rich sediments. An even better correlation is seen when plotting Zr/Al against Si/Al to eliminate the dilution effect of biogenic carbonate (Fig. 4b). In this case, all three sediment types show high correlation, with $R > 0.91$. It is noteworthy that carbonate-dominated sediment trends to generally lower Zr/Al values compared to the more siliciclastic sediments for any given value of Si/Al. This behaviour is consistent with zircon being mostly enriched in silty and sandy deposits rather than the carbonate-rich sediments whose siliciclastic fraction is inferred to be slightly more silt-poor and sand-rich relative to other sediments at a given Si/Al value (Jonell *et al.* 2018). In this case, Zr/Al is more of relative silt content rather than discharge power.

We plot both K/Al and K/Rb against Si/Al to determine if the chemical weathering proxies are related to lithology or mineralogy (Fig. 7). Figure 7a shows that there is little correlation between K/Al and Si/Al ($R = 0.0042$), with the bulk of the sediments clustered with low values in both ratios. However, silt/clay-rich sediments show a better positive linear correlation, with less alteration (higher K/Al values) correlating with greater proportions of quartz grains ($R = 0.5700$), as might be expected. Although it is possible that the different size fractions have contrasting provenance that might account for these differences, our data cannot constrain this. However, bulk sediment Nd and Sr isotope data from the Indus Delta indicate that provenance does not have a very strong effect (Jonell *et al.* 2018). It is interesting to note that Si/Al values at Site U1456 are generally higher than the average of the Holocene Indus Delta (Si/Al = 3.87) (Clift *et al.* 2010) and the Holocene Indus Canyon (Si/Al = 3.53 (Li *et al.* 2018)), suggestive of a systematic

offset perhaps caused by the analytical method, likely low efficiency of Al fluorescence during scanning. This is surprising given the distal, muddy character of the sediments at Site U1456 compared to the sandier delta. In contrast, K/Al values are generally lower in the Laxmi Basin than the 0.193 average of the Holocene delta and the 0.191 of the Holocene canyon. The greater alteration that this implies is consistent with the finer-grained character of the sediments in the distal fan location. Comparison of Miocene sediments with the Holocene delta and canyon may not be entirely valid given the change in provenance and climate that has occurred in the intervening time period (Clift *et al.* 2018).

Stronger alteration is more associated with fine rather than coarser-grained material unless weathering is very strong and removes most of the degraded minerals and mobile elements, leaving only quartz-rich sand. However, K/Rb shows a more consistent negative correlation with Si/Al (Fig. 7b) ($R = 0.5177$), especially when only considering the sand-rich sediments ($R = 0.7921$), but not the clay/silt-rich sediment ($R = 0.2619$). At any given Si/Al value, K/Rb is higher in carbonate-dominated sediments than in sand-dominated sediments, i.e. the clastic fraction of the carbonate-dominated sediments is less altered than that in sandy sediment. Higher sand flux associated with more chemical alteration is potentially linked to wetter terrestrial environments. This trend indicates that sediments with higher Si/Al values have lower K/Rb values, i.e. sandy sediment is preferentially depleted in K relative to Rb. K-feldspar and biotite contain about the same amount of K (8–10 wt %), but biotite usually contains more Rb (500–1000 ppm) than K-feldspar (400–600 ppm) (Hanson, 1978) and is prone to more rapid breakdown during early chemical weathering (Blum & Erel, 1997). K-feldspar also tends to release Rb more quickly than K in the early stages of chemical weathering, but as the process continues, preferential K loss dominates (Nesbitt *et al.* 1980). This means that K/Rb of the sediment may first rise and then fall as weathering proceeds, especially in the presence of abundant biotite.

We explored the relationship between K/Rb and mineralogy further by plotting K/Rb against Rb (Fig. 8a). This shows no overall

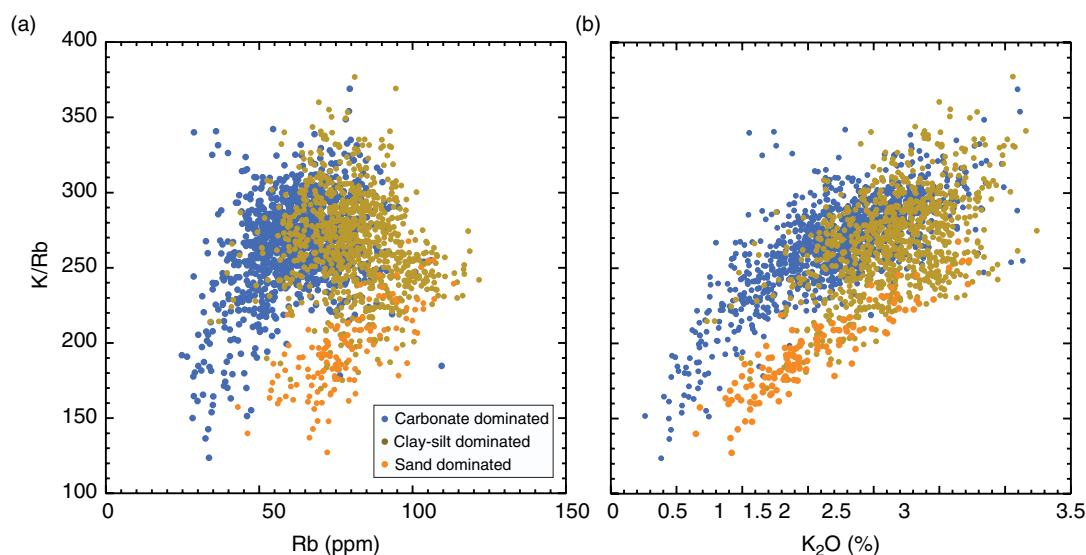


Fig. 8. Cross-plot of K/Rb vs Rb showing some linearity between these factors in sand-dominated sediments but not in finer-grained material. Ratios are calculated from weight ppm of oxides.

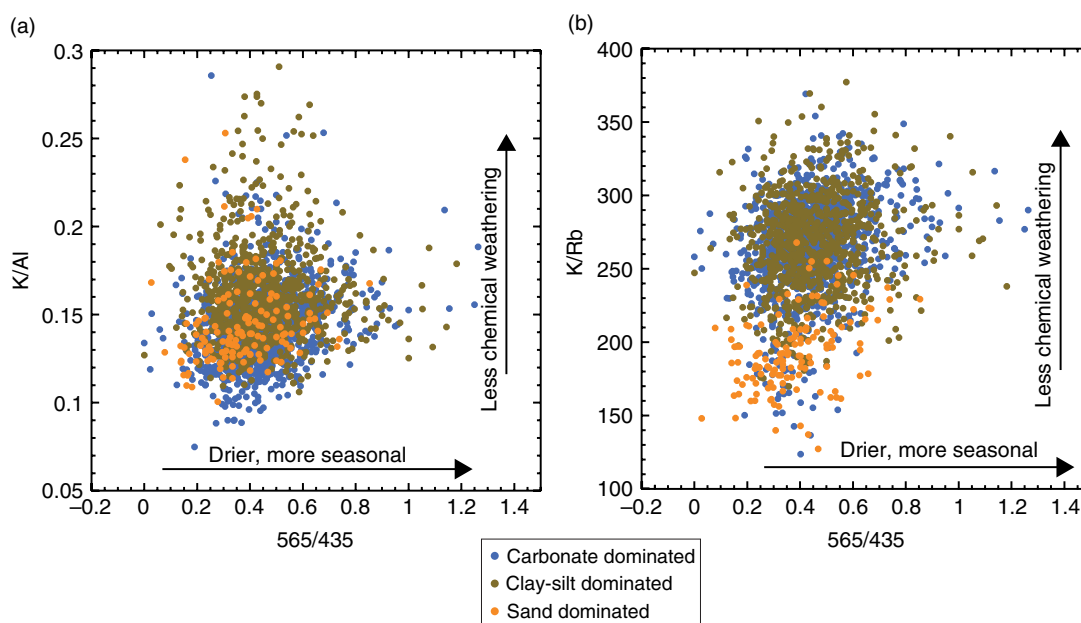


Fig. 9. Cross-plots of 565/435 against (a) K/Al and (b) K/Rb. Ratios are calculated from wt % and ppm of oxides.

pattern ($R = 0.0260$), but there is a rough positive correlation if we only consider sand-dominated sediment ($R = 0.0320$). This means that K/Rb is not controlled by Rb abundance in the sand grains, which would drive a negative correlation. There is no apparent trend like this in the clay/silt-rich or carbonate sediments. The links between K_2O and K/Rb are better defined (Fig. 8b) ($R = 0.4456$), with the poorest correlation for the clay/silt-rich sediments ($R = 0.3425$). The offset of the carbonate-dominated sediments to lower K_2O value for a given K/Rb value reflects the dilution effect of the biogenic carbonate on total concentration. The overall positive correlation implies that it is loss of K relative to Rb that drives the variations observed in K/Rb and that advanced chemical weathering of K-feldspars dominates over biotite, with Rb behaving in a less mobile fashion than K. We do note, however, that Rb varies in a

regular fashion in the section and that abundances are not very low. The K/Rb proxy can be considered a more reliable indicator of weathering intensity in sandy sediment than K/Al.

7.a. Weathering, erosion and humidity

We also compare these chemical weathering proxies with the 565/435 hematite/goethite proxy (Fig. 9). K/Al does not correlate coherently with 565/435, and little difference is seen among the three major lithology categories. In general, the lowest values of K/Al, implying strong degrees of chemical weathering, are more associated with low concentration of hematite relative to goethite ($565/435 < 0.6$) and thus potentially more humid conditions. This association is slightly better shown as a plot of K/Rb vs 565/435

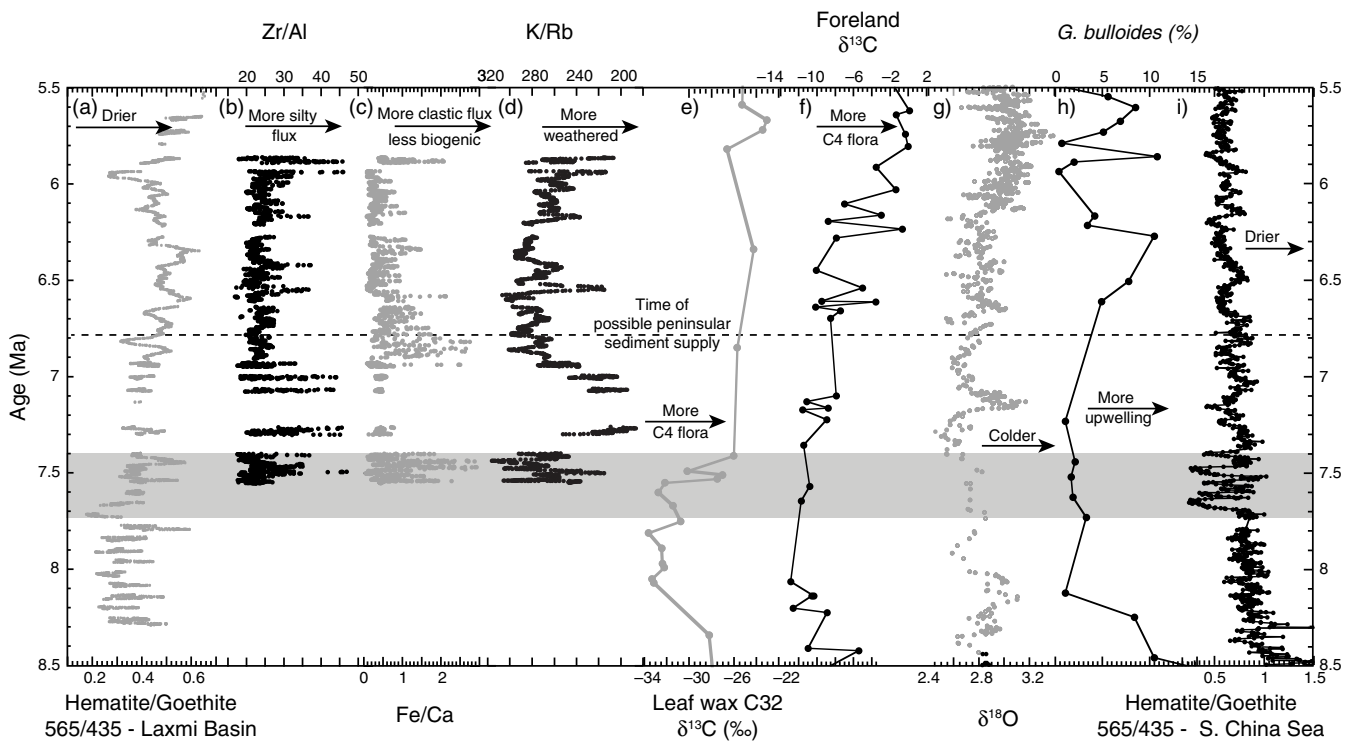


Fig. 10. Plot of proxy evolution from 8.5 to 5.5 Ma. (a) Hematite/goethite from 565/435, (b) Zr/Al ($\times 10^4$) as a proxy for terrestrial clastic flux / grain size, (c) Fe/Ca clastic flux vs biogenic production, (d) K/Rb as a proxy for degree of chemical weathering, (e) $\delta^{13}\text{C}$ from C32 leaf waxes at Site U1456 (Suzuki *et al.* 2019), (f) foreland $\delta^{13}\text{C}$ from soil carbonates (Quade *et al.* 1989), (g) benthic foraminifer $\delta^{18}\text{O}$ from global compilation (Zachos *et al.* 2001), (h) *G. bulloides* abundance as a monsoon-related upwelling proxy from ODP Site 722 (Huang *et al.* 2007), and (i) hematite/goethite from 565/435 from ODP Site 1148 in the northern South China Sea.

(Fig. 9b) ($R = 0.2161$), although the data are clustered over a relatively small range of values. This plot shows that the sand-rich sediments are more altered than the finer-grained sediments and are associated with lower hematite/goethite values (average 0.354) compared with silt/clay-rich sediments (average 0.450). Wetter, less seasonal conditions (565/435 < 0.5) are more associated with the lowest values of K/Rb (average 257 and minimum of 123), indicating that the greatest degrees of chemical weathering are linked to the wettest / least seasonal conditions, although weakly weathered sediments may also be found under these conditions. The most hematite-rich sediments with the highest values of 565/435 (> 0.8) are associated with relatively high values of K/Rb (average 280 and minimum of 221), indicating less chemical alteration overall during times of dry or seasonal environmental conditions. K/Rb data imply that the strongest chemical weathering is associated with the most humid conditions and potentially with the strongest summer monsoon rains.

The relationship between the degree of weathering, erosion and climate is not linear. Giosan *et al.* (2017) have shown that mass flux rates during the Holocene increase as run-off increases but also when precipitation decreases and vegetation cover decreases. On a longer timescale, weathering is seen to decrease with a weaker monsoon in the Arabian Sea and South China Sea, while increasing in the Bengal Fan (Clift *et al.* 2008b). Here we suggest that wetter and less seasonal climate increases the degree of alteration, but that total alteration decreases as transport times shorten with stronger discharge, resulting in less time for alteration to occur. As climate dried and became more seasonal during the Late Miocene, there is a long-term shift to less chemical weathering. The driest conditions are not linked to strong alteration.

7.b. Temporal evolution

The evolution of erosion, weathering and environmental properties can be compared with other well-accepted measures of monsoon intensity spanning the studied time interval (Fig. 10). The 565/435 proxy shows an overall long-term increase in hematite relative to goethite, implying greater aridity, especially starting around 7.7 Ma and continuing until 6.4 Ma. Although temperature, as well as moisture, is important in controlling the relative abundance of hematite vs goethite, these factors can be hard to separate because of a lack of a good continental temperature proxy. If we use the marine oxygen isotope record of Zachos *et al.* (2001) as a guide to temperatures and ice volumes then we see that long-term cooling and ice growth (Herbert *et al.* 2016) mirrors the relative increase in hematite. However, it is noteworthy that in some intervals the $\delta^{18}\text{O}$ record does correlate with some of the other proxies over short timescales. Between 6.2 and 5.7 Ma, the $\delta^{18}\text{O}$ values increased, implying colder conditions, whereas at the same time 565/435 decreased indicating relatively less hematite. This relationship argues for humidity being dominant over temperature in controlling this proxy.

A simple interpretation of the 565/435 proxy suggests increasing humidity until 5.95 Ma, after which time the environment dried again. The geochemical data do not extend into sediments older than 7.6 Ma, but it is clear that between 7.6 and 6.9 Ma there was significant variability and high silt-sized clastic flux (larger grain size), as measured by Zr/Al. This was followed by decreasing silt-sized clastic flux to relatively low levels from 6.9 Ma until 5.95 Ma, at a time when some sediment may be derived from the Indian margin to the east (Clift *et al.* 2018). After that time, there was again a resurgence

towards higher values. The observed pattern demonstrates that there is significant variability but that in general high siliciclastic flux is almost always associated with times of wetter environmental conditions, whereas the drier climate between 6.9 and 5.95 Ma is linked with a low rate of clastic flux.

It is noteworthy that at 7.4–7.6 Ma, both Zr/Al and Fe/Ca indicate strong silt-sized clastic flux relative to biogenic production. However, from 7.4 to 6.95 Ma, Fe/Ca was low despite scattered high values of Zr/Al, implying a time of enhanced biogenic production. Conversely, from 6.95 to 6.4 Ma, Fe/Ca values were high whereas Zr/Al was low, implying low silt-sized clastic flux and either very low biogenic production and/or a dominantly clay-rich clastic flux. This corresponds with a section of carbonate-poor sediment in the core (Fig. 2). After 6.4 Ma the two proxies are more in accord with one another and indicate more clastic relative to biogenic production at a time of enhanced silty sedimentation. This requires that during that time it was the clastic flux from the Indus River that controlled Fe/Ca values.

The weathering response to climate change is more complex, but in general K/Rb shows lower values, indicating more chemical weathering at a time when the clastic flux was high, which in turn correlates with a trend to more humid conditions based on the 565/435 values. This correlation is in accord with the concept that wetter conditions allow chemical weathering to proceed at a faster rate than arid conditions. We note that from 7.0 Ma to c. 6.6 Ma, the 565/435 values increased as K/Rb increased, whereas after that time 565/435 decreased, suggesting an increasingly wet environment from 6.6 to 5.95 Ma as chemical weathering intensified (lower K/Rb) values.

7.c. Comparison with existing proxies

The long-term trend from 7.7 to 5.6 Ma was toward relatively more hematite, with short-lived excursions to wetter conditions and less hematite relative to goethite. We note that this trend is consistent with $\delta^{13}\text{C}$ data from carbonate nodules and palaeosols in the Pakistani Himalayan foreland that show a long-term shift towards more C4 grassland vegetation at that time (Quade *et al.* 1989). The $\delta^{13}\text{C}$ data derived from leaf waxes from Site U1456 also show the same trend (Suzuki *et al.* 2019) (Fig. 10). We would compare this trend with the geochemically defined chemical weathering intensity, but the XRF data do not extend deep enough to demonstrate what the compositions were before the transition to drier conditions after 7.7 Ma. However, there are high K/Rb values and mostly low Zr/Al values, during the climate transition, indicative of weak chemical weathering and physical erosion. The intensification of both these processes after that time occurs when we have no detailed $\delta^{13}\text{C}$ data from Laxmi Basin, so it is impossible to say whether that change represents an opposite weathering/erosion response or if there was a brief relapse to wetter conditions after c. 7.4 Ma. The 565/435 data do not show much change after 7.4 Ma, and lithology also does not change significantly. Existing isotopic controls are not sufficient to show whether this excursion might be driven by a change in provenance.

We further compare our results with monsoon-related oceanic upwelling records from the Oman margin derived from ODP Site 722 (Fig. 10) (Huang *et al.* 2007). These show an increase in *G. bulloides* after 6.6 Ma compared to the period before 7.2 Ma (Fig. 10h). 6.6 to 6.25 Ma was a time of increasing aridity and weaker chemical weathering according to our proxies (Fig. 10a, d). This is consistent with analyses that the wind-based monsoon proxies from the western Arabian Sea are not good rainfall proxies for the Himalayan foreland (Clift, 2017). The same trend to more

upwelling but a drier, hematite-rich environment onshore is seen between 6.0 and 5.6 Ma, and a peak in upwelling from 6.25 to 6.5 Ma (Fig. 10h) is also a time of high 565/435. This demonstrates that upwelling-related winds are strongest when the climate was driest, not wettest, as might be expected from the modern situation in this region.

What controls these environmental and palaeoceanographic trends? In general during the Quaternary the summer monsoon rains are strongest during interglacial periods and weak during the Last Glacial Maximum, so a correlation with global climate is justified (Fleitmann *et al.* 2003; Rohling *et al.* 2009). There is a long-term trend to colder global temperatures after 7.0 Ma, based on benthic foraminiferal oxygen isotope data (Fig. 10g) (Zachos *et al.* 2001). The brief spike to colder temperatures seen at 7.2–7.1 Ma has no age-equivalent sediments at Site U1456, but the changes in erosion and weathering reconstructed between 7.5 and 6.9 Ma do not correlate with any major global climate changes.

From 7.6 to 6.7 Ma the Fe/Ca values (terrestrial flux vs biogenic production proxy) appear to be largely anticorrelated with Zr/Al (silt vs clay proxy) and K/Rb (weathering proxy) (Fig. 10b–d). Thus when the rate of terrestrial sediment supply was low compared to biogenic carbonate production, both the chemical weathering and the silt content of the sediment were high. This occurred coeval with the C3 to C4 transition occurring in the Indus flood plains (Quade *et al.* 1989) (Fig. 10f) and shortly after a sharp rise in leaf wax $\delta^{13}\text{C}$ values (Fig. 10e), both indicators of drying of the terrestrial environment. Weaker rains could slow sediment transport across the plains and increase sediment alteration, while reduced vegetation cover might expedite erosion of silty flood plains during seasonal summer rains (Giosan *et al.* 2017). The reduction in Fe/Ca would then correlate with greater biogenic production rather than enhanced total terrestrial sediment discharge.

The long-term trend to increased weathering and sandy siliciclastic flux from 6.4 to 5.9 Ma is likewise a time of drying (more hematite vs goethite), which is associated with global climatic cooling at that time. Cooling might be expected to drive drying, reduce fluvial discharge and slow transport of sediment across the flood plains. However, the faster erosion and weathering observed would be predicted if aridity and seasonality increased to the point that vegetation was sparse and seasonal flash flooding increased net erosion (Molnar, 2001; Giosan *et al.* 2017).

Although the intensity of the SW monsoon is linked to mountain uplift and especially to the height of the Himalayan barrier (Boos & Kuang, 2010), the decrease in rainfall intensity over the studied interval is probably not related to changes in this parameter or to the tectonics of the Himalaya / Tibetan Plateau. Most geological lines of evidence presently favour relatively early Palaeogene uplift of the southern Tibetan Plateau (Spicer *et al.* 2003; Harris, 2006; Rowley & Currie, 2006), and although there is some indication of decreased altitude in SW Tibet this is dated to the Pliocene, too late to have potentially influenced the climatic trends reconstructed here (Saylor *et al.* 2009). The late Miocene was largely marked by exhumation of the Lesser Himalaya and the growth of the Lesser Himalayan Duplex (Huyghe *et al.* 2001; Najman *et al.* 2009), but this is not linked to a change in height of the topographic barrier and is thus not expected to have affected rainfall intensity or the environments of the Indus flood plains.

Finally we compare our environmental trend with data from the same time period in the South China Sea (Fig. 10i). The sediment at ODP Site 1148 is interpreted to have been derived from southern China, largely from a palaeo-Pearl River basin (Clift *et al.* 2008b) and is also strongly affected by summer monsoon rains. Although

this is the East and not the South Asian monsoon, they might largely co-vary because they share several of the same external forcing processes, such as global climate and the elevation of the Tibetan Plateau (Kutzbach *et al.* 1993; Molnar *et al.* 1993). The trend to higher 565/435 at Site U1456 between 7.7 and 6.4 Ma was a time of steadily falling 565/435 values at Site 1148 (Fig. 10a, i). The trend in 565/435 in the South China Sea is consistent with a strengthening summer monsoon, which in turn matches the *G. bulloides* upwelling record from the Arabian Sea. We consider it likely that aridity changed in different ways in different parts of Asia. The increase in leaf wax $\delta^{13}\text{C}$ seen around 7.5 Ma at Site U1456 (Fig. 10e) (Suzuki *et al.* 2019) is consistent with the 565/435 record at the same site but is noted as a time of strongly lower 565/435 at Site 1148, implying wetter conditions in southern China as the climate dried in South Asia.

Do these data imply that the East Asian monsoon intensified as the SW monsoon dried? This is a possibility based on these data alone, but other factors suggest more plausible alternatives. An increase in aeolian sedimentation in the Chinese Loess Plateau and the North Pacific after 8 Ma argues for more drying in central Asia at that time (Rea *et al.* 1998; An *et al.* 2000), and sediment grain-size and clay mineral data from the South China Sea have been interpreted to reflect a stronger winter monsoon relative to summer monsoon after 8 Ma (Wan *et al.* 2007). The drying of northern and central China at the same time that the Indus Basin dried does not, however, preclude wetter conditions in southern China, possibly caused by a southward migration of the Intertropical Convergence Zone (ITCZ). However, this seems unlikely because palaeo-salinity records from the northern South China Sea show increasing salinity after 7.5 Ma, implying less runoff and a weaker summer monsoon in southern China at that time (Steinke *et al.* 2010). Southern China is now significantly wetter than Pakistan and western India, and increased goethite formation relative to hematite might occur if rainfall had become less seasonal in southern China during the late Miocene. Total rainfall could have reduced while remaining still wet enough to form goethite due to precipitation in both winter and summer. We further speculate that the different topography of southern China (low hilly country), compared with the high mountains of the western Himalaya and Karakoram, adjacent to the long alluvial plains of the Indus may have caused a different weathering and erosional response to the climate change. With monsoon rainfall concentrated against the mountain front in the Himalayas (Bookhagen & Burbank, 2006), the flood plains could remain relatively dry and suitable for hematite formation, while this situation would not be possible in the more hilly regions of southern China.

8. Conclusions

We used a combination of XRF core scanning data and DRS spectral data to constrain development of chemical weathering, terrestrial erosive flux and the relative humidity of the Indus plains from 8.5 to 5.5 Ma using sediment recovered from the Indus Fan at IODP Site U1456 in the Laxmi Basin, eastern Arabian Sea. Among the weathering proxies, K/Al shows relatively modest degrees of change up-section, whereas K/Rb is more sensitive to changes in weathering intensity. K/Rb shows a long-term decrease with time from 7.5 to 5.7 Ma, but with large coherent variations. This latter proxy is also partly controlled by the sandiness of the section. Our data imply less chemical weathering during times when sedimentation was more carbonate-dominated, especially around 6.5 Ma within the overall trend to decreasing weathering

intensity. K/Rb variations relative to the 565/435 hematite/goethite proxy indicate less chemical weathering during times of lower humidity, but variable weathering when humidity was higher. Physical erosion proxies Si/Al and Zr/Al do not show a clear link to aridity beyond the observation that times of intense aridity are also times of lower siliciclastic flux. An interval of strong chemical weathering and physical erosion flux from 7.3 to 6.9 Ma is not mirrored by changes in 565/435.

A long-term trend to higher 565/435 from 7.7 to 6.3 Ma indicates drying, especially when coupled with both foreland and marine $\delta^{13}\text{C}$ isotope records that document a shift to more C4 grassland vegetation, linked to more arid conditions during the late Miocene (Quade *et al.* 1989; Singh *et al.* 2011). The long-term environmental trend parallels and is likely driven by falling global seawater temperatures rather than being triggered by tectonics or the changing height of the Himalayan topographic barrier or the Tibetan Plateau. The hematite/goethite record is at odds with upwelling records from the Oman margin that show heightened biogenic productivity and thus wind strength, but which do not constrain rainfall in the Indus Basin. The long-term trend in hematite/goethite reconstructed at Site U1456 is the opposite of that previously found in the northern South China Sea at the same time, and is probably linked to reduced seasonality in the presence of a generally wetter climate and in the absence of a dry, extensive alluvial plain such as seen in the Indus Basin. The contrasting weathering responses in these two regions reflect differences in the topography and overall climate of the drainage basins.

Supplementary material. To view supplementary material for this article, please visit <https://doi.org/10.1017/S0016756819000608>.

Author ORCIDs. Peter D. Clift 0001-6660-6388; Denise K Kulhanek, 0000-0002-2156-6383; Annette Hahn, 0000-0002-3647-473X

Acknowledgements. This research used samples and data provided by the International Ocean Discovery Program (IODP). Funding for this research was provided by the US Science Support Program (USSSP) from National Science Foundation (NSF) award 1450528 to Lamont-Doherty/Columbia University. Additional funding came from the Charles T McCord Jr Chair in Petroleum Geology at Louisiana State University.

References

- An Z, Sun D, Chen M, Sun Y, Li L and Chen B (2000) Red clay sequences in the Chinese Loess Plateau and paleoclimate events of the upper Tertiary. *Disiji Yanjiu = Quaternary Sciences* 20, 435–46.
- Bahr A, Jiménez-Espejo FJ, Kolasinac N, Grunert P, Hernández-Molina FJ, Röhl U, Voelker AHL, Escutia C, Stow DAV, Hodell D and Alvarez-Zarikian CA (2014) Deciphering bottom current velocity and paleoclimate signals from contourite deposits in the Gulf of Cádiz during the last 140 kyr: an inorganic geochemical approach. *Geochemistry, Geophysics, Geosystems* 15, 3145–60. doi: 10.1002/2014GC005356.
- Balsam WL, Damuth JE, Schneider RR and Fox GL (1997) Comparison of shipboard vs. shore-based spectral data from Amazon fan cores: implications for interpreting sediment composition. In *Proceedings of the Ocean Drilling Program, Scientific Results, vol. 155* (eds RD Flood, DJW Piper, A Klaus and LC Peterson), pp. 193–215. College Station, Texas: Ocean Drilling Program.
- Berner RA and Berner EK (1997) Silicate weathering and climate. In *Tectonic Uplift and Climate Change* (ed. WF Ruddiman), pp. 353–65. New York: Springer.
- Betzler C, Eberli GP, Kroon D, Wright JD, Swart PK, Nath BN, Alvarez-Zarikian CA, Alonso-García M, Bialik OM, Blättler CL, Guo JA, Haffen S, Horozai S, Inoue M, Jovane L, Lanci L, Laya JC, Mee ALH, Lüdmann T, Nakakuni M, Niino K, Petruny LM, Pratihi SD, Reijmer JGG, Reolid J, Slagle AL, Sloss CR, Su X, Yao Z and Young JR (2016)

- The abrupt onset of the modern South Asian Monsoon winds. *Scientific Reports* **6**, 29838. doi: [10.1038/srep29838](https://doi.org/10.1038/srep29838).
- Bhattacharya GCB, Chaubey AK, Murty GPS, Srinivas S, Sarma KV, Subrahmanyam V and Krishna KS** (1994) Evidence for seafloor spreading in the Laxmi Basin, northeastern Indian Ocean. *Earth and Planetary Science Letters* **125**, 211–20.
- Blum JD and Erel Y** (1997) Rb/Sr isotope systematics of a granitic soil chronosequence: the importance of biotite weathering. *Geochimica et Cosmochimica Acta* **61**, 3193–204. doi: [10.1016/S0016-7037\(97\)00148-8](https://doi.org/10.1016/S0016-7037(97)00148-8).
- Bookhagen B and Burbank DW** (2006) Topography, relief, and TRMM-derived rainfall variations along the Himalaya. *Geophysical Research Letters* **33**, L08405. doi: [10.1029/2006GL026037](https://doi.org/10.1029/2006GL026037).
- Boos WR and Kuang Z** (2010) Dominant control of the South Asian monsoon by orographic insulation versus plateau heating. *Nature* **463**, 218–22. doi: [10.1038/nature08707](https://doi.org/10.1038/nature08707).
- Burbank DW, Beck RA and Mulder T** (1996) The Himalayan foreland basin. In *The Tectonics of Asia* (eds A Yin and TM Harrison), pp. 149–88. New York: Cambridge University Press.
- Burbank DW, Blythe AE, Putkonen J, Pratt-Sitaula B, Gabet E, Oskins M, Barros A and Ojha TP** (2003) Decoupling of erosion and precipitation in the Himalayas. *Nature* **426**, 652–5.
- Burbank DW, Derry LA and France-Lanord C** (1993) Reduced Himalayan sediment production 8 Myr ago despite an intensified monsoon. *Nature* **364**, 48–50.
- Burdige DJ** (1993) The biogeochemistry of manganese and iron reduction in marine sediments. *Earth-Science Reviews* **35**, 249–84. doi: [10.1016/0012-8252\(93\)90040-E](https://doi.org/10.1016/0012-8252(93)90040-E).
- Clift PD** (2017) Cenozoic sedimentary records of climate-tectonic coupling in the Western Himalaya. *Progress in Earth and Planetary Science* **4**, 1–22. doi: [10.1186/s40645-017-0151-8](https://doi.org/10.1186/s40645-017-0151-8).
- Clift PD, Giosan L, Blusztajn J, Campbell IH, Allen CM, Pringle M, Tabrez A, Danish M, Rabbani MM, Carter A and Lückge A** (2008a) Holocene erosion of the Lesser Himalaya triggered by intensified summer monsoon. *Geology* **36**, 79–82. doi: [10.1130/G24315A.1](https://doi.org/10.1130/G24315A.1).
- Clift PD, Giosan L, Carter A, Garzanti E, Galy V, Tabrez AR, Pringle M, Campbell IH, France-Lanord C, Blusztajn J, Allen C, Alizai A, Lückge A, Danish M and Rabbani MM** (2010) Monsoon control over erosion patterns in the Western Himalaya: possible feed-backs into the tectonic evolution. In *Monsoon Evolution and Tectonic–Climate Linkage in Asia* (eds PD Clift, R Tada and H Zheng), pp. 181–213. Geological Society of London, Special Publication no. 342.
- Clift PD, Hodges K, Heslop D, Hannigan R, Hoang LV and Calves G** (2008b) Greater Himalayan exhumation triggered by Early Miocene monsoon intensification. *Nature Geoscience* **1**, 875–80. doi: [10.1038/ngeo351](https://doi.org/10.1038/ngeo351).
- Clift PD, Shimizu N, Layne G, Gaedicke C, Schlüter HU, Clark MK and Amjad S** (2001) Development of the Indus Fan and its significance for the erosional history of the western Himalaya and Karakoram. *Geological Society of America Bulletin* **113**, 1039–51.
- Clift PD, Wan S and Blusztajn J** (2014) Reconstructing chemical weathering, physical erosion and monsoon intensity since 25 Ma in the northern South China Sea: a review of competing proxies. *Earth-Science Reviews* **130**, 86–102. doi: [10.1016/j.earscirev.2014.01.002](https://doi.org/10.1016/j.earscirev.2014.01.002).
- Clift PD, Zhou P, Stockli DF and Blusztajn J** (2018) Regional pliocene exhumation of the lesser Himalaya in the Indus Drainage. *Solid Earth* **10**, 647–61. doi: [10.5194/se-2018-132](https://doi.org/10.5194/se-2018-132).
- Curry WB, Ostermann DR, Guptha MVS and Ittekkot V** (1992) Foraminiferal production and monsoonal upwelling in the Arabian Sea; evidence from sediment traps. In *Upwelling Systems; Evolution since the Early Miocene* (eds CP Summerhayes, WL Prell and KC Emeis), pp. 93–106. Geological Society of London, Special Publication no. 64.
- DeCelles PG, Kapp P, Gehrels GE and Ding L** (2014) Paleocene-Eocene foreland basin evolution in the Himalaya of southern Tibet and Nepal: implications for the age of initial India-Asia collision. *Tectonics* **33**, 824–49. doi: [10.1002/2014TC003522](https://doi.org/10.1002/2014TC003522).
- East AE, Clift PD, Carter A, Alizai A and VanLaningham S** (2015) Fluvial-aeolian interactions in sediment routing and sedimentary signal buffering: an example from the Indus Basin and Thar Desert. *Journal of Sedimentary Research* **85**, 715–28. doi: [10.2110/jsr.2015.42](https://doi.org/10.2110/jsr.2015.42).
- Fleitmann D, Burns SJ, Mudelsee M, Neff U, Kramers J, Mangini A and Matter A** (2003) Holocene forcing of the Indian monsoon recorded in a stalagmite from southern Oman. *Science* **300**, 1737–9.
- Galy V, France-Lanord C, Beyssac O, Faure P, Kudrass H-R and Palhol F** (2007) Efficient organic carbon burial in the Bengal fan sustained by the Himalayan erosional system. *Nature* **450**, 407–11. doi: [10.1038/nature06273](https://doi.org/10.1038/nature06273).
- Giosan L, Flood RD, Grutzner J and Mudie P** (2002) Paleoclimatographic significance of sediment color on western North Atlantic Drifts: II. Late Pliocene-Pleistocene sedimentation. *Marine Geology* **189**, 43–61.
- Giosan L, Ponton C, Usman M, Blusztajn J, Fuller DQ, Galy V, Haghpor N, Johnson JE, McIntyre C, Wacker L and Eglinton TI** (2017) Short communication: massive erosion in monsoonal central India linked to late Holocene land cover degradation. *Earth Surface Dynamics* **5**, 781–9. doi: [10.5194/esurf-5-781-2017](https://doi.org/10.5194/esurf-5-781-2017).
- Govin A, Holzwarth U, Heslop D, Keeling LF, Zabel M, Mulitza S, Collins JA and Chiessi CM** (2012) Distribution of major elements in Atlantic surface sediments (36°N–49°S): imprint of terrigenous input and continental weathering. *Geochemistry, Geophysics, Geosystems* **13**, Q01013. doi: [10.1029/2011GC003785](https://doi.org/10.1029/2011GC003785).
- Gupta AK, Yuvaraja A, Prakasam M, Clemens SC and Velu A** (2015) Evolution of the South Asian monsoon wind system since the late Middle Miocene. *Palaeogeography, Palaeoclimatology, Palaeoecology* **438**, 160–7. doi: [10.1016/j.palaeo.2015.08.006](https://doi.org/10.1016/j.palaeo.2015.08.006).
- Hahn A, Bowen MG, Clift PD, Kulhanek DK, Lyle MW and Zabel M** (2019) Testing the analytical performance of handheld XRF using marine sediments of IODP Expedition 355. *Geological Magazine* **156**, 1–5. doi: [10.1017/S0016756819000189](https://doi.org/10.1017/S0016756819000189).
- Hanson GN** (1978) The application of trace elements to the petrogenesis of igneous rocks of granitic composition. *Earth and Planetary Science Letters* **38**, 26–43. doi: [10.1016/0012-821X\(78\)90124-3](https://doi.org/10.1016/0012-821X(78)90124-3).
- Harris NBW** (2006) The elevation of the Tibetan Plateau and its impact on the monsoon. *Palaeogeography, Palaeoclimatology, Palaeoecology* **241**, 4–15.
- Herbert TD, Lawrence KT, Tzanova A, Peterson LC, Caballero-Gill R and Kelly CS** (2016) Late Miocene global cooling and the rise of modern ecosystems. *Nature Geoscience* **9**, 843–7. doi: [10.1038/ngeo2813](https://doi.org/10.1038/ngeo2813).
- Honjo S, Dymond J, Prell W and Ittekkot V** (1999) Monsoon controlled export fluxes to the interior of the Arabian Sea. *Deep-Sea Research II* **46**, 1859–902.
- Hu D, Clift PD, Wan S, Böning P, Hannigan R, Hillier S and Blusztajn J** (2016) Testing chemical weathering proxies in Miocene–Recent fluvial-derived sediments in the South China Sea. In *River-Dominated Shelf Sediments of East Asian Seas* (eds PD Clift, J Harff, J Wu and Y Qiu). Geological Society of London, Special Publication no. 429.
- Huang Y, Clemens SC, Liu W, Wang Y and Prell WL** (2007) Large-scale hydrological change drove the late Miocene C4 plant expansion in the Himalayan foreland and Arabian Peninsula. *Geology* **35**, 531–4.
- Huyghe P, Galy A, Mugnier J-L and France-Lanord C** (2001) Propagation of the thrust system and erosion in the Lesser Himalaya: geochemical and sedimentological evidence. *Geology* **29**, 1007–10.
- Ji J, Balsam W, Chen JU and Liu L** (2002) Rapid and quantitative measurement of hematite and goethite in the Chinese loess-paleosol sequence by diffuse reflectance spectroscopy. *Clays and Clay Minerals* **50**, 208–16. doi: [10.1346/000986002760832801](https://doi.org/10.1346/000986002760832801).
- Jonell TN, Li Y, Blusztajn J, Giosan L and Clift PD** (2018) Signal or noise? Isolating grain size effects on Nd and Sr isotope variability in Indus delta sediment provenance. *Chemical Geology* **485**, 56–73. doi: [10.1016/j.chemgeo.2018.03.036](https://doi.org/10.1016/j.chemgeo.2018.03.036).
- Karim A and Veizer J** (2002) Water balance of the Indus river basin and moisture source in the Karakoram and western Himalayas: implications from hydrogen and oxygen isotopes river water. *Journal of Geophysical Research* **107**, 4362. doi: [10.1029/2000JD000253](https://doi.org/10.1029/2000JD000253).
- Kido Y, Koshikawa T and Tada R** (2006) Rapid and quantitative major element analysis method for wet fine-grained sediments using an XRF microscanner. *Marine Geology* **229**, 209–25.
- Kolla V and Coumes F** (1987) Morphology, internal structure, seismic stratigraphy, and sedimentation of Indus Fan. *AAPG Bulletin* **71**, 650–77.
- Kroon D, Steens T and Troelstra SR** (1991) Onset of Monsoonal related upwelling in the western Arabian Sea as revealed by planktonic foraminifers.

- In *Proceedings of the Ocean Drilling Program, Scientific Results, vol. 117* (eds W Prell N Niitsuma), pp. 257–63. College Station, Texas: Ocean Drilling Program.
- Kump LR, Brantley SL and Arthur MA** (2000) Chemical weathering, atmospheric CO₂, and climate. *Annual Review of Earth and Planetary Sciences* **28**, 611–67.
- Kutzbach JE, Prell WL and Ruddiman WF** (1993) Sensitivity of Eurasian climate to surface uplift of the Tibetan Plateau. *Journal of Geology* **101**, 177–90.
- Li Y, Clift PD, Böning P, Blusztajn J, Murray RW, Ireland T, Pahnke K and Giosan L** (2018) Continuous signal propagation in the Indus Submarine Canyon since the Last Deglacial. *Marine Geology* **406**, 159–76. doi: [10.1016/j.margeo.2018.09.011](https://doi.org/10.1016/j.margeo.2018.09.011).
- Lupker M, France-Lanord C, Galy V, Lave J, Gaillardet J, Gajured AP, Guilmette C, Rahman M, Singh SK and Sinha R** (2012) Predominant flood-plain over mountain weathering of Himalayan sediments (Ganga basin). *Geochimica et Cosmochimica Acta* **84**, 410–32.
- Lupker M, France-Lanord C, Galy V, Lave J and Kudrass H** (2013) Increasing chemical weathering in the Himalayan system since the Last Glacial Maximum. *Earth and Planetary Science Letters* **365**, 243–52.
- Lyle M, Kulhanek DK, Bowen MG and Hahn A** (2018) Data report: X-ray fluorescence studies of Site U1457 sediments, Laxmi Basin, Arabian Sea. *Proceedings of the International Ocean Discovery Program* **355**. doi: [10.14379/iodp.proc.355.203.2018](https://doi.org/10.14379/iodp.proc.355.203.2018).
- Lyle M, Olivarez Lyle A, Gorgas T, Holbourn A, Westerhold T, Hathorne E, Kimoto K and Yamamoto S** (2012) Data report: raw and normalized elemental data along the Site U1338 splice from X-ray fluorescence scanning. *Proceedings of the Integrated Ocean Drilling Program* **320/321**. doi: [10.2204/iodp.proc.320321.203.2012](https://doi.org/10.2204/iodp.proc.320321.203.2012).
- Miles PR and Roest WR** (1993) Earliest sea-floor spreading magnetic anomalies in the north Arabian Sea and the ocean-continent transition. *Geophysical Journal International* **115**, 1025–31.
- Molnar P** (2001) Climate change, flooding in arid environments, and erosion rates. *Geology* **29**, 1071–4.
- Molnar P, England P and Martinod J** (1993) Mantle dynamics, uplift of the Tibetan Plateau, and the Indian Monsoon. *Reviews of Geophysics* **31**, 357–96.
- Najman Y** (2006) The detrital record of orogenesis: a review of approaches and techniques used in the Himalayan sedimentary basins. *Earth-Science Reviews* **74**, 1–72.
- Najman Y, Appel E, Boudagher-Fadel M, Bown P, Carter A, Garzanti E, Godin L, Han J, Liebke U, Oliver G, Parrish R and Vezzoli G** (2010) Timing of India-Asia collision: geological, biostratigraphic, and palaeomagnetic constraints. *Journal of Geophysical Research* **115**, B12416. doi: [10.1029/2010JB007673](https://doi.org/10.1029/2010JB007673).
- Najman Y, Bickle M, Garzanti E, Pringle M, Barfod D, Brozovic N, Burbank D and Ando S** (2009) Reconstructing the exhumation history of the Lesser Himalaya, NW India, from a multitechnique provenance study of the foreland basin Siwalik Group. *Tectonics* **28**, TC5018. doi: [10.1029/2009TC002506](https://doi.org/10.1029/2009TC002506).
- Nesbitt HW, Markovics G and Price RC** (1980) Chemical processes affecting alkalis and alkaline earths during continental weathering. *Geochimica et Cosmochimica Acta* **44**, 1659–66.
- Olde K, Jarvis I, Uličný D, Pearce MA, Trabucho-Alexandre J, Čech S, Gröcke DR, Laurin J, Švábenická L and Tocher BA** (2015) Geochemical and palynological sea-level proxies in hemipelagic sediments: a critical assessment from the Upper Cretaceous of the Czech Republic. *Palaeogeography, Palaeoclimatology, Palaeoecology* **435**, 222–43. doi: [10.1016/j.palaeo.2015.06.018](https://doi.org/10.1016/j.palaeo.2015.06.018).
- Pandey DK, Clift PD, Kulhanek DK, Andò S, Bendle JAP, Bratenkov S, Griffith EM, Gurumurthy GP, Hahn A, Iwai M, Khim B-K, Kumar A, Kumar AG, Liddy HM, Lu H, Lyle MW, Mishra R, Radhakrishna T, Routledge CM, Saraswat R, Saxena R, Scardia G, Sharma GK, Singh AD, Steinke S, Suzuki K, Tauxe L, Tiwari M, Xu Z and Yu Z** (2016a) Site U1456. In *Arabian Sea Monsoon. Proceedings of the International Ocean Discovery Program, vol. 355* (eds DK Pandey, PD Clift, DK Kulhanek and Expedition 355 Scientists). pp. 1–61. College Station, Texas: International Ocean Discovery Program. doi: [10.14379/iodp.proc.355.103.2016](https://doi.org/10.14379/iodp.proc.355.103.2016).
- Pandey DK, Clift PD, Kulhanek DK** and Expedition 355 Scientists (2016b) *Arabian Sea Monsoon. Proceedings of the International Ocean Discovery Program, vol. 355*. pp. 1–10. College Station, Texas: International Ocean Discovery Program. doi: [10.14379/iodp.proc.355.2016](https://doi.org/10.14379/iodp.proc.355.2016).
- Pandey OP, Agrawal PK and Negi JG** (1995) Lithospheric structure beneath Laxmi Ridge and late Cretaceous geodynamic events. *Geo-Marine Letters* **15**, 85–91.
- Pease PP, Tchakerian VP and Tindale NW** (1998) Aerosols over the Arabian Sea: geochemistry and source areas for aeolian desert dust. *Journal of Arid Environments* **39**, 477–96. doi: [10.1006/jare.1997.0368](https://doi.org/10.1006/jare.1997.0368).
- Prell WL, Murray DW, Clemens SC and Anderson DM** (1992) Evolution and variability of the Indian Ocean Summer Monsoon: evidence from the western Arabian Sea drilling program. In *Synthesis of Results from Scientific Drilling in the Indian Ocean* (eds RA Duncan, DK Rea, RB Kidd, U von Rad JK Weissel), pp. 447–69. Washington, DC: American Geophysical Union. Geophysical Monograph, 70.
- Quade J, Cerling TE and Bowman JR** (1989) Development of Asian monsoon revealed by marked ecological shift during the latest Miocene in northern Pakistan. *Nature* **342**, 163–6.
- Raymo ME and Ruddiman WF** (1992) Tectonic forcing of Late Cenozoic climate. *Nature* **359**, 117–22.
- Rea DK, Snoeckx H and Joseph LH** (1998) Late Cenozoic eolian deposition in the North Pacific: Asian drying, Tibetan uplift, and cooling of the northern hemisphere. *Paleoceanography* **13**, 215–24.
- Reiners PW, Ehlers TA, Mitchell SG and Montgomery DR** (2003) Coupled spatial variations in precipitation and long-term erosion rates across the Washington Cascades. *Nature* **426**, 645–7.
- Richter TO, van der Gaast S, Koster B, Vaars A, Giele R, de Stigter HC, De Haas H and van Weering TCE** (2006) The Avaatech XRF Core Scanner: technical description and applications to NE Atlantic sediments. In *New Techniques in Sediment Core Analysis* (ed. RG Rothwell), pp. 39–50. Geological Society of London, Special Publication no. 267.
- Riebe CS, Kirchner JW and Finkel RC** (2004) Erosional and climatic effects in long-term chemical weathering rates in granitic landscapes spanning diverse climate regimes. *Earth and Planetary Science Letters* **224**, 547–62.
- Robinson SG, Sahota JTS and Oldfield F** (2000) Early diagenesis in North Atlantic abyssal plain sediments characterized by rock-magnetic and geochemical indices. *Marine Geology* **163**, 77–107. doi: [10.1016/S0025-3227\(99\)00108-5](https://doi.org/10.1016/S0025-3227(99)00108-5).
- Rohling EJ, Liu QS, Roberts AP, Stanford JD, Rasmussen SO, Langen PL and Siddall M** (2009) Controls on the East Asian monsoon during the last glacial cycle, based on comparison between Hulu Cave and polar ice-core records. *Quaternary Science Reviews* **28**, 3291–302. doi: [10.1016/j.quascirev.2009.09.007](https://doi.org/10.1016/j.quascirev.2009.09.007).
- Routledge CM, Kulhanek DK, Tauxe L, Scardia G, Singh AD, Steinke S, Griffith EM and Saraswat R** (2019) A revised chronostratigraphic framework for International Ocean Discovery Program Expedition 355 sites in Laxmi basin, eastern Arabian Sea. *Geological Magazine* **156**, 1–18. doi: [10.1017/S0016756819000104](https://doi.org/10.1017/S0016756819000104).
- Rowley DB and Currie BS** (2006) Palaeo-altimetry of the late Eocene to Miocene Lunpola basin, central Tibet. *Nature* **439**, 677–81.
- Sangode SJ and Bloemendal J** (2004) Pedogenic transformation of magnetic minerals in Pliocene-Pleistocene palaeosols of the Siwalik Group, NW Himalaya, India. *Palaeogeography, Palaeoclimatology, Palaeoecology* **212**, 95–118.
- Saylor JE, Quade J, Dettman DL, DeCelles PG, Kapp PA and Ding L** (2009) The Late Miocene through present paleoelevation history of southwestern Tibet. *American Journal of Science* **309**, 1–42.
- Schnetger B, Brumsack HJ, Schale H, Hinrichs J and Dittert L** (2000) Geochemical characteristics of deep-sea sediments from the Arabian Sea: a high-resolution study. *Deep Sea Research Part II: Topical Studies in Oceanography* **47**, 2735–68. doi: [10.1016/S0967-0645\(00\)00047-3](https://doi.org/10.1016/S0967-0645(00)00047-3).
- Schwertmann U** (1971) Transformation of hematite to goethite in soils. *Nature* **232**, 624–5.
- Singh S, Parkash B, Awasthi AK and Kumar S** (2011) Late Miocene record of palaeovegetation from Siwalik palaeosols of the Ramnagar sub-basin, India. *Current Science* **100**, 213–22.
- Singhvi AK, Williams MAJ, Rajaguru SN, Misra VN, Chawla S, Stokes S, Chauhan N, Francis T, Ganjoo RK and Humphreys GS** (2010) A 200 ka record of climatic change and dune activity in the Thar Desert, India.

- Quaternary Science Reviews* **29**, 3095–105. doi: [10.1016/j.quascirev.2010.08.003](https://doi.org/10.1016/j.quascirev.2010.08.003).
- Spicer RA, Harris NBW, Widdowson M, Herman AB, Guo S, Valdes PJ, Wolfe JA and Kelley SP** (2003) Constant elevation of southern Tibet over the past 15 million years. *Nature* **421**, 622–4.
- Steinke S, Groeneveld J, Johnstone H and Rendle-Bühning R** (2010) East Asian summer monsoon weakening after 7.5 Ma: evidence from combined planktonic foraminifera Mg/Ca and $\delta^{18}\text{O}$ (ODP Site 1146; northern South China Sea). *Palaeogeography, Palaeoclimatology, Palaeoecology* **289**, 33–43. doi: [10.1016/j.palaeo.2010.02.007](https://doi.org/10.1016/j.palaeo.2010.02.007).
- Suzuki K, Yamamoto M and Seki O** (2019) Stable isotopic evolution of leaf waxes from IODP Site U1456. *Geological Magazine* **156**.
- Tada R, Zheng H and Clift PD** (2016) Evolution and variability of the Asian monsoon and its potential linkage with uplift of the Himalaya and Tibetan Plateau. *Progress in Earth and Planetary Science* **3**, 1–26. doi: [10.1186/s40645-016-0080-y](https://doi.org/10.1186/s40645-016-0080-y).
- Tauxe L and Opdyke ND** (1982) A time framework based on magnetostratigraphy of the Siwalik sediments of the Khaur area, northern Pakistan. *Palaeogeography, Palaeoclimatology, Palaeoecology* **37**, 43–61.
- Taylor SR and McLennan SM** (1995) The geochemical evolution of the continental crust. *Reviews of Geophysics* **33**, 241–65.
- Vögeli N, Najman Y, Beek PVD, Huyghe P, Wynn PM, Govin G, Veen IVD and Sachse D** (2017) Lateral variations in vegetation in the Himalaya since the Miocene and implications for climate evolution. *Earth and Planetary Science Letters* **471**, 1–9. doi: [10.1016/j.epsl.2017.04.037](https://doi.org/10.1016/j.epsl.2017.04.037).
- Wan S, Clift PD, Zhao D, Hovius N, Munhoven G, France-Lanord C, Wang Y, Xiong Z, Huang J, Yu Z, Zhang J, Ma W, Zhang G, Li A and Li T** (2017) Enhanced silicate weathering of tropical shelf sediments exposed during glacial lowstands: a sink for atmospheric CO_2 . *Geochimica et Cosmochimica Acta* **200**, 123–44. doi: [10.1016/j.gca.2016.12.010](https://doi.org/10.1016/j.gca.2016.12.010).
- Wan S, Li A, Clift PD and Stuut J-BW** (2007) Development of the East Asian monsoon: mineralogical and sedimentologic records in the northern South China Sea since 20 Ma. *Palaeogeography, Palaeoclimatology, Palaeoecology* **254**, 561–82.
- West AJ, Galy A and Bickle MJ** (2005) Tectonic and climatic controls on silicate weathering. *Earth and Planetary Science Letters* **235**, 211–28. doi: [10.1016/j.epsl.2005.03.020](https://doi.org/10.1016/j.epsl.2005.03.020).
- Weltje GJ, Bloemsma MR, Tjallingii R, Heslop D, Röhl U and Croudace IW** (2015) Prediction of geochemical composition from XRF core scanner data: a new multivariate approach including automatic selection of calibration samples and quantification of uncertainties. In *Micro-XRF Studies of Sediment Cores: Applications of a non-destructive tool for the environmental sciences* (eds IW Croudace and RG Rothwell), pp. 507–534. Dordrecht: Springer Netherlands.
- Whipple KX and Tucker GE** (1999) Dynamics of the stream-power river incision model: implications for height limits of mountain ranges, landscape response timescales, and research needs. *Journal of Geophysical Research: Solid Earth* **104**, 17661–74.
- Zachos J, Pagani M, Sloan L, Thomas E and Billups K** (2001) Trends, rhythms and aberrations in global climate 65 Ma to Present. *Science* **292**, 686–93.